

# Progress and investigation on lattice Boltzmann modeling of multiple immiscible fluids or components with variable density and viscosity ratios

Sébastien Leclaire\*, Marcelo Reggio, Jean-Yves Trépanier

Department of Mechanical Engineering, École Polytechnique, 2500, chemin de Polytechnique, Montreal, Quebec, Canada H3T 1J4

## ARTICLE INFO

### Article history:

Received 10 December 2011

Received in revised form 17 July 2012

Accepted 22 March 2013

Available online 4 April 2013

### Keywords:

Lattice Boltzmann method

Multiphase flow

Multicomponent flow

Rothman–Keller type

Fundamental validations

High density ratio

High viscosity ratio

## ABSTRACT

Lattice Boltzmann models for simulating multiphase flows are relatively new, and much work remains to be done to demonstrate their ability to solve fundamental test cases before they are considered for engineering problems. From this perspective, a hydrodynamic lattice Boltzmann model for simulating immiscible multiphase flows with high density and high viscosity ratios, up to  $O(1000)$  and  $O(100)$  respectively, is presented and validated against analytical solutions. The method is based on a two phase flow model with operators extended to handle  $N$  immiscible fluids. The current approach is  $O(N)$  in computational complexity for the number of different gradient approximations. This is a major improvement, considering the  $O(N^2)$  complexity found in most works. A sequence of systematic and essential tests have been conducted to establish milestones that need to be met by the proposed approach (as well as by other methods). First, the method is validated qualitatively by demonstrating its ability to address the spinodal decomposition of immiscible fluids. Second, the model is quantitatively verified for the case of multilayered planar interfaces. Third, the multiphase Laplace law is studied for the case of three fluids. Fourth, a quality index is developed for the three-phase Laplace–Young's law, which concerns the position of the interfaces between the fluids resulting from the different surface tensions. The current model is compatible with the analytical solution, and is shown to be first order accurate in terms of this quality index. Finally, the multilayered Couette's flow is studied. In this study, numerical results can recover the analytical solutions for all the selected test cases, as long as unit density ratios are considered. For high density and high viscosity ratios, the analytical solution is recovered for all tests, except that of the multilayered Couette's flow. Numerical results and a discussion are presented for this unsuccessful test case. It is believed that other LB models may have the same problem in addressing the simulation of multiphase flows with variable density ratios.

© 2013 Elsevier Inc. All rights reserved.

## 1. Introduction

Two decades ago, the lattice Boltzmann (LB) model for simulating immiscible fluids was derived from the cellular automata model [1]. Shortly after that, Gunstensen and Rothman [2] adapted the idea of Rothman and Keller (RK) [1], and created an LB model for immiscible two phase flows. This type of model (RK) uses color gradients to separate and model the interaction at the interface of the fluids. Another idea for simulating immiscible fluids was developed by Shan and Chen [3] (SC),

\* Corresponding author.

E-mail address: [sebastien.leclaire@polymtl.ca](mailto:sebastien.leclaire@polymtl.ca) (S. Leclaire).

which consisted of introducing an effective mass function to simulate the interaction between the fluids. A third method was presented by Swift et al. [4], where collision rules are chosen to ensure that the system evolves towards the minimum of an input free energy (FE) functional. A fourth method, the mean-field (MF) method, simulate interparticle attraction in the same way as the Coulomb interaction is treated in the Vlasov equation [5]. Finally, the field mediator (FM) methods use null mass particles, the only role of which is to invert the momentum of lattice particles in the transition layer to segregate fluids of different colors [6]. Each of these five models, RK [1,2], SC [3], FE [4], MF [5], and FM [6], belongs to one class of LB model for simulating immiscible two phase flows. It is worth noting that this classification is not universal, and that there are other methods, not discussed in this work, which may not be classified among those mentioned above. Recent work by Bao and Schaefer [7] allowed multiphase and multicomponent flow with high density ratios using the SC approach. A recent and more complete literature review is presented by Gokaltun and McDaniel [8] on LB modeling designed to simulate flow with both high density and high viscosity ratios.

In this work, an RK type LB model based on the Reis and Phillips [9] approach is studied. Grunau et al. [10] have removed some of the limitations of the original RK model of Gunstensen and Rothman [2] by introducing variable density and viscosity ratios. However, the Grunau et al. model can only simulate very low density or viscosity ratios. A major improvement was the redefinition of the recoloring operator, which is incorporated into the model to segregate the fluids. D'Ortona et al. [11] reported that spurious currents were significantly reduced with the new recoloring operator. Later, Latva-Kokko and Rothman [12] modified D'Ortona et al.'s recoloring operator to avoid a negative probability distribution. The new recoloring operator also substantially reduced the “lattice pinning” problem [12]. Recently, Reis and Phillips [9] made an important contribution to the RK model, which was to adapt the model of Grunau et al. [10] for the popular D2Q9 lattice. Most importantly, they managed to construct a perturbation operator which introduces the surface tension in a way that is compatible, within the macroscopic limit, with the form of the capillary stress tensor. For some test cases, their model is able to simulate higher density ratios than previous RK models, even when neither the recoloring operator of D'Ortona et al. [11] nor that of Latva-Kokko and Rothman [12] is used. More recently, Leclaire et al. [13] have adapted the recoloring operator of Latva-Kokko and Rothman to the Reis and Phillips [9] model. Doing so has substantially increased the density ratio between the fluids for several test cases, and the noise in the model has been reduced in such a way that numerical steady state solutions have become possible. In addition, Leclaire et al. [14] showed that, by using an isotropic gradient discretization for the color gradient, it is possible to accurately simulate Laplace's law with density ratios as high as 10000. Moreover, the spurious currents are significantly reduced and accurate simulations with a very low surface tension are possible. With these latter results, the accuracy and range of the model parameters have been greatly improved in the RK model.

Still, in the lattice Boltzmann RK model, much less attention has been paid to the simulation of multiphase flows with three or more fluids. The first study on this topic was presented in the Ph.D. thesis of Gunstensen [15]. His model has limitations, however, because the method for extending the two-phase model to its three-phase counterpart cannot be generalized, nor is it obvious how it could be generalized to  $N$ -phase flows. The approach works well for three phases, but only because there are only three fluid–fluid interfaces, which is equal to the number of fluids. Because this model was introduced almost 20 years ago, it does not contain any of the improvements subsequently made to the RK model. Another RK-based model for simulating multicomponent flows is that of Dupin et al. [16]. By defining a color gradient for each of the fluid–fluid interfaces, they avoided the problem that someone may encounter when attempting to generalize to  $N$ -phase the Gunstensen model [15]. A similar alternative was offered by Halliday et al. [17], in which a possible generalization of the recoloring operator is presented for  $N$  phases. A more recent version, similar to the Halliday et al. model, is described by Spencer et al. [18]. Unfortunately, none of these multiphase models was built to simulate variable density ratios. In this paper, we introduce a model that does do so, by consolidating the applicability and advantages of two-phase flows into an  $N$ -phase flow model.

In order to improve the model's ability to simulate high density ratios, we incorporated high-order isotropic gradient discretization for the color gradient computed at each time step. As previously shown [14], this kind of discretization increases the accuracy of the model [14]. Because of the cost associated with gradient computing, this model is designed to reduce, as much as possible, the number of different gradient approximations to be calculated. As stated by Halliday et al. [17], gradient calculation is a source of a significant computational overhead, to the point where these authors decided to consider local gradient approximation when the interface curvature is small. The basis of this approach allows us to consider generalization to  $N$ -phase flows, with the number of different gradient approximations  $O(N)$  in computational complexity, i.e. neighbor information is needed only with  $O(N)$  complexity. This is a clear improvement over most models, which are  $O(N^2)$  in complexity [17,18].

In a previous RK model [16], the computational complexity was shown to be reduced from  $O(N^2)$  to  $O(\approx 5)$  by neglecting the effect of some fluids. This procedure could also be applied here to obtain similar results. However, if all the fluid interactions must be taken into account, then  $O(N)$  complexity is preferable to  $O(N^2)$ .

This paper is organized in two major sections. First, the LB model for  $N$  immiscible fluids is presented. Novel numerical details of the model requirements are given and discussed throughout this work. Then, various numerical simulations for multiphase flows are introduced, performed, and analyzed. When possible, the results are compared with the available analytical solutions for multiphase flows. This new multiphase RK model is able to simulate large density and viscosity ratios, up to  $O(1000)$  and  $O(100)$  respectively, for all but one of the selected test cases. The unsuccessful test case for variable density ratios is the multilayered Couette's flow. Numerical results and an investigation are presented for this test case in Section (3.5).

## 2. Lattice Boltzmann immiscible multiphase model

The current LB approach follows the two-phase model of Reis and Phillips [9], along with the improvements presented by Leclaire et al. [13,14] for the recoloring operator and the color gradient. For this 2D LB model, conceptually, there are  $N$  sets of distribution functions, one for each fluid, moving on a D2Q9 lattice with the velocity vectors  $\vec{c}_i$ . We say conceptually, because, in reality, only the color-blind set of distribution functions is needed (see Section (4) for technical details). With  $\Delta x = \Delta y = 1$  and  $\theta_i = \frac{\pi}{4}(4 - i)$ , the velocity vectors are defined as:

$$\vec{c}_i = \begin{cases} (0, 0), & i = 1 \\ [\sin(\theta_i), \cos(\theta_i)], & i = 2, 4, 6, 8 \\ [\sin(\theta_i), \cos(\theta_i)]\sqrt{2}, & i = 3, 5, 7, 9 \end{cases} \quad (1)$$

The distribution functions for a fluid of color  $k$  (e.g.  $k = r$  for red,  $k = g$  for green, and  $k = b$  for blue) are noted  $N_i^k(\vec{x}, t)$ , while  $N_i(\vec{x}, t) = \sum_k N_i^k(\vec{x}, t)$  is used for the color-blind distribution function. If the time step is  $\Delta t = 1$ , the algorithm uses the following evolution equation:

$$N_i^k(\vec{x} + \vec{c}_i, t + 1) = N_i^k(\vec{x}, t) + \Omega_i^k(N_i^k(\vec{x}, t)) \quad (2)$$

where the collision operator  $\Omega_i^k$  is the result of the combination of three sub operators (similar to Ref. [19]):

$$\Omega_i^k = (\Omega_i^k)^{(3)} \left[ (\Omega_i^k)^{(1)} + (\Omega_i^k)^{(2)} \right] \quad (3)$$

The evolution equation is solved in four steps with operator splitting, as follows:

1. Single phase collision operator (BGK):  $N_i^k(\vec{x}, t_*) = (\Omega_i^k)^{(1)}(N_i^k(\vec{x}, t))$
2. Multiphase collision operator (perturbation):  $N_i^k(\vec{x}, t_{**}) = (\Omega_i^k)^{(2)}(N_i^k(\vec{x}, t_*))$
3. Multiphase collision operator (recoloring):  $N_i^k(\vec{x}, t_{***}) = (\Omega_i^k)^{(3)}(N_i^k(\vec{x}, t_{**}))$
4. Streaming operator:  $N_i^k(\vec{x} + \vec{c}_i, t + 1) = N_i^k(\vec{x}, t_{***})$

### 2.1. Single phase collision operator

The first sub operator,  $(\Omega_i^k)^{(1)}$ , is the standard BGK operator of the single phase LB model, where the distribution functions are relaxed towards a local equilibrium, in which  $\omega_{\text{eff}}$  denotes the effective relaxation factor:

$$(\Omega_i^k)^{(1)}(N_i^k) = N_i^k - \omega_{\text{eff}}(N_i^k - N_i^{k(e)}) \quad (4)$$

The details of this operator are the following. The density of the fluid  $k$  is given by the first moment of the distribution functions:

$$\rho_k = \sum_i N_i^k = \sum_i N_i^{k(e)} \quad (5)$$

where the superscript  $(e)$  denotes equilibrium. The total fluid density is given by  $\rho = \sum_k \rho_k$ , while the total momentum is defined as the second moment of the distribution functions:

$$\rho \vec{u} = \sum_i \sum_k N_i^k \vec{c}_i = \sum_i \sum_k N_i^{k(e)} \vec{c}_i \quad (6)$$

in which  $\vec{u}$  is the density weighted arithmetic average velocity of the fluid. The equilibrium functions are defined by [9]:

$$N_i^{k(e)}(\rho_k, \vec{u}, \alpha_k) = \rho_k \left( \phi_i^k + W_i \left[ 3\vec{c}_i \cdot \vec{u} + \frac{9}{2}(\vec{c}_i \cdot \vec{u})^2 - \frac{3}{2}(\vec{u})^2 \right] \right) \quad (7)$$

These equilibrium distribution functions  $N_i^{k(e)}$  are chosen to satisfy the principles of conservation of mass and momentum. The weights  $W_i$  are those of a standard D2Q9 lattice:

$$W_i = \begin{cases} 4/9, & i = 1 \\ 1/9, & i = 2, 4, 6, 8 \\ 1/36, & i = 3, 5, 7, 9 \end{cases} \quad (8)$$

Besides,

$$\phi_i^k = \begin{cases} \alpha_k, & i = 1 \\ (1 - \alpha_k)/5, & i = 2, 4, 6, 8 \\ (1 - \alpha_k)/20, & i = 3, 5, 7, 9 \end{cases} \quad (9)$$

As introduced in Ref. [10] for two-phase flows, the different density ratios between  $k$  and  $l$  fluids are  $\gamma_{kl}$ , and must be taken as follows to obtain a stable interface:

$$\gamma_{kl} = \frac{\rho_k^0}{\rho_l^0} = \frac{1 - \alpha_l}{1 - \alpha_k} \quad (10)$$

where the superscript “0” over  $\rho_k^0$  indicates the initial value of  $\rho_k$  at the beginning of the simulation.

The pressure of the fluid of color  $k$  is:

$$p^k = \frac{3\rho_k(1 - \alpha_k)}{5} = \rho_k(c_s^k)^2 \quad (11)$$

In the above expressions, one of the  $\alpha_k$  represents a free parameter. We let  $\kappa$  be the index of the least dense fluid. Generally, we set the value of  $\alpha_\kappa > 0$ , then the relation  $0 < \alpha_\kappa \leq \alpha_k < 1$  is guaranteed to hold for each fluid  $k$ . These parameters set the sound speed  $c_s^k$  in each fluid of color  $k$  [9].

The effective relaxation parameter  $\omega_{\text{eff}}$  is chosen so that the evolution equation, Eq. (2), respects the macroscopic equations for a single-phase flow in the single-phase regions. When the viscosities of the fluids are different, an interpolation is applied to define the parameter  $\omega_{\text{eff}}$  at the interface. For flows with more than two phases, it is easier to consider only a simple interpolation, which is different from the quadratic-type interpolation from the basic two phase flow model [9,10]. It is very important to note that  $\omega_{\text{eff}}$  must be the same for each fluid, since, without it, the amount of computer memory required for this model is much larger. If  $\omega_{\text{eff}}$  is not the same for each fluid color, the distribution functions of each fluid color will need to be kept in the computer memory, instead of only the color blind distribution functions as it is explained in Section (4).

In this paper, we define the bar functional as the density weighted  $q$ -average. For example, for a variable  $X_k$  defined for each fluid  $k$ , the density weighted  $q$ -average of this variable is defined as:

$$\bar{X}|_q = \begin{cases} \left( \sum_k \frac{\rho_k (X_k)^q}{\rho} \right)^{\frac{1}{q}}, & q \neq 0 \\ \left( \prod_k (X_k)^{\rho_k} \right)^{\frac{1}{\rho}}, & q = 0 \end{cases} \quad (12)$$

If  $\nu_k$  is the kinematic viscosity of the fluid  $k$ , then, depending on the  $q$ -average, one possible choice for the effective relaxation parameter is:

$$\omega_{\text{eff}} = \frac{1}{3(\bar{\nu}|_q) + \frac{1}{2}} \quad (13)$$

The choice to define  $\omega_{\text{eff}}$  in this way is not the only option, and, since the accuracy of the model seems to greatly depend on that choice, different choices for  $\omega_{\text{eff}}$  are investigated in this study, namely the  $q$ -average with  $q = -1, 0, 1$  and  $2$ .

As will be discussed further in Sections (3.2) and (3.5) concerning the multilayered planar interface and the multilayered Couette's flow, none of the effective relaxation parameters  $\omega_{\text{eff}}$  studied here seems to be the perfect candidate in all circumstances. Nevertheless, from these two test cases, we suggest that  $q = -1$  is the best choice when simulating unit density ratios, while  $q = 1$  appears to be a better choice when non unit density ratios are treated. We note that depending on what is important, e.g. surface tension or velocity, other alternatives for  $q$  could lead to better results. In the work of Refs. [16,20,19], when three or more phases are simulated,  $q = 1$  is used.

## 2.2. Perturbation operator

In the RK model, surface tension is modeled by means of the perturbation operator [2,9,21]. First, to introduce the surface tension into this model, a “color” gradient  $\vec{F}$  that approximates the interface normal needs to be defined for each of the fluid–fluid interfaces.

The first possibility that may be considered is the natural extension for  $N$  phases of the color gradient present in the basic two phase model [14]:

$$\vec{F}_{kl}^{\text{natural}} = \vec{\nabla}(\rho_k - \rho_l) \quad (14)$$

According to this form, the number of different gradient approximations is  $O(N^2)$  in complexity, because one gradient approximation for each interface needs to be computed at each lattice site. This follows from the number of possible interfaces in a  $N$ -phase flow, which is equal to  $N(N - 1)/2$ . Instead of applying the gradient operator to the density difference, it is also possible to distribute the gradient operator to each fluid density, in order to obtain:

$$\vec{F}_{kl}^{\text{natural}} = \vec{\nabla}\rho_k - \vec{\nabla}\rho_l \quad (15)$$

Clearly, the number of different gradient approximations is now  $O(N)$  in complexity. Only one gradient approximation for each phase needs to be computed at each lattice site. Note that, in this particular case, the two color gradients in Eqs. (14) and (15) are analytically/numerically equivalent.

Unfortunately, the color gradient in Eq. (15) leads to non physical results when three or more phases are simulated. In fact, in Section (3.3.1), it is shown that this natural extension leads to a non physical mass flow along the direction tangential to the interfaces.

Another possible color gradient or phase field gradient is the one presented in the model of Spencer et al. [18]:

$$\vec{F}_{kl}^{phase} = \vec{\nabla} \left( \frac{\rho_k - \rho_l}{\rho_k + \rho_l} \right) \quad (16)$$

Once more, this color gradient is  $O(N^2)$  in complexity for the number of different gradient approximations. It is again possible to distribute the gradient operator to obtain a color gradient that is  $O(N)$  in complexity:

$$\vec{F}_{kl}^{phase} = 2 \frac{\rho_l \vec{\nabla} \rho_k - \rho_k \vec{\nabla} \rho_l}{(\rho_k + \rho_l)^2} \quad (17)$$

It is important to note that this time the two gradients in Eqs. (16) and (17) are not numerically equal, because the discrete gradient operator is a linear combination of stencil values, while the color gradient  $\vec{F}_{kl}^{phase}$  in Eq. (17) is not a linear combination of the density gradients. Therefore, the results that would be obtained in a simulation using Eq. (16) will not be the same as with Eq. (17). It should be noted that the color gradient  $\vec{F}_{kl}^{phase}$  is undefined when both fluids  $\rho_k$  and  $\rho_l$  are absent. This situation arises when three or more phases occur. This phase field gradient is clearly suited to two-phase flows, but will be prone to numerical instability and inaccuracy when three or more phases occur.

For this model, we found only one color gradient  $O(N)$  in complexity that leads to physical results and not prone to numerical instability. Based on the Allen–Cahn system [22], the color gradient in this model is defined as:

$$\vec{F}_{kl} = \frac{\rho_l}{\rho} \vec{\nabla} \left( \frac{\rho_k}{\rho} \right) - \frac{\rho_k}{\rho} \vec{\nabla} \left( \frac{\rho_l}{\rho} \right) \quad (18)$$

It is interesting to note that the color gradient in Eq. (18) from the Allen–Cahn system is very similar to the phase field gradient in Eq. (17). In fact, it can be shown that for two-phase flows these two gradients are exactly the same, except that the color gradient  $\vec{F}_{kl}^{phase}$  is twice the length of  $\vec{F}_{kl}$ . Therefore, we can conclude that the gradient  $\vec{F}_{kl}$  is a more rigorous generalization for  $N$ -phase flows than  $\vec{F}_{kl}^{phase}$ , because  $\vec{F}_{kl}$  is a vector function that is always defined.

In order not to neglect any fluid interaction,  $O(N)$  complexity is preferable when the number of phases is growing. Therefore, the way the algorithm is implemented is very important. Specifically, if  $N$  different gradient approximations need to be computed with the same stencils for every lattice site, this can be achieved very quickly using convolution products and storing them in computer memory for future use [23]. This is an important point we are making in this paper, and one that becomes increasingly important as the order of the gradient discretization grows. Also, high-order gradient discretization is preferred in some cases, in order to accurately simulate high density ratios with this type of model [14]. In this work, an eighth order isotropic discrete gradient operator is used for the gradient of the density fraction  $\rho_k/\rho$  of each fluid. More details about this isotropic discrete gradient operator are given in Section (2.4).

The perturbation operator, for the fluid  $k$ , is therefore defined by:

$$(\Omega_i^k)^{(2)}(N_i^k) = N_i^k + \sum_{l \neq k} \frac{A_{kl} C_{kl}}{2} |\vec{F}_{kl}| \left[ W_i \frac{(\vec{F}_{kl} \cdot \vec{C}_i)^2}{|\vec{F}_{kl}|^2} - B_i \right] \quad (19)$$

where

$$B_i = \begin{cases} -4/27, & i = 1 \\ 2/27, & i = 2, 4, 6, 8 \\ 5/108, & i = 3, 5, 7, 9 \end{cases} \quad (20)$$

and

$$C_{kl} = \min \left\{ \eta_1 \frac{\rho_k \rho_l}{\rho_k^0 \rho_l^0}, 1 \right\} \quad (21)$$

where  $\eta_1 = 10^6$  is a threshold and the function  $C_{kl}$  is a concentration factor that limits the activation of the surface tension at the  $k$ - $l$  interface only where both the  $k$  and  $l$  fluids are present. The accuracy of the model depends on the choice of  $\eta_1$ , but its effect appears to be very small for a very wide range of values. To our knowledge, this is the first time that the concentration factor in Eq. (21) has been used. There are other concentration factors in the literature, in the work of Dupin et al. [16], for example:

$$C_{kl} = 1 - \frac{|\rho_k - \rho_l|}{|\rho_k + \rho_l|} \quad (22)$$

Again, it can be noted that, for three or more phases, this concentration factor can be undefined over some regions of the computational domain.

Reis and Phillips [9] have shown that the perturbation operator complies, within the macroscopic limit, with the capillary stress tensor present in the macroscopic equations for two-phase flows. It handles the coupling between the two fluids, with the space- and time-dependent parameters  $A_{kl}$  chosen to model the surface tension between the  $k$ - $l$  fluid interface. Although this operator generates the surface tension, it does not guarantee the fluid's immiscibility. To minimize the mixing and segregate the fluids, the recoloring operator  $(\Omega_i^k)^{(3)}$  needs to be properly selected.

### 2.3. Recoloring operator

This last operator is used to maximize the amount of fluid of color  $k$  at the interface that is sent to the  $k$  fluid region, while respecting the conservation of mass and total momentum. The recoloring operator presented here is a combination of the essential ideas from Latva-Kokko and Rothman [12] and Halliday et al. [17]:

$$(\Omega_i^k)^{(3)}(N_i^k) = \frac{\rho_k}{\rho} N_i + \sum_{l \neq k} \beta_{kl} \frac{\rho_k \rho_l}{\rho^2} \cos(\varphi_i^{kl}) N_i^{(e)}(\rho, \mathbf{0}, \bar{\alpha}|_{q=1}) \quad (23)$$

where  $\beta_{kl}$  is a parameter controlling the thickness of the  $k$ - $l$  interface [12]. The variable  $\varphi_i^{kl}$  corresponds to the angle between the color gradient  $\vec{F}_{kl}$  and the lattice direction vector  $\vec{c}_i$ . The equilibrium distributions of the color-blind fluid  $N_i^{(e)}$  in Eq. (23) are evaluated using Eq. (7), a zero velocity, and the respective value of  $\bar{\alpha}|_{q=1}$ . It should be noted that, for  $i = 1$ , there is a division by 0. In such a case, the numerator is also 0, and we release the indetermination by setting the whole term equal to 0 to respect mass conservation. Also, the parameter  $\beta_{kl}$  must be between 0 and 1 to ensure, at least for a two-fluid interface, that the distribution functions remain positive [12]. When three or more fluids are present at an interface, it is not clear whether or not the distribution functions will remain positive, but the current numerical results seem to indicate that the numerical evolution of the solution is stable with  $0 \leq \beta_{kl} \leq 1$ . Moreover, it should also be noted that  $\beta_{kl} = \beta_{lk}$ , in order to guarantee mass and momentum conservation.

### 2.4. Isotropic discrete gradient operator

In this work, an eighth order isotropic discrete gradient operator is used. This kind of gradient operator was generalized by Sbragaglia et al. for 2D and 3D higher order isotropic operators [24]. In Ref. [14], it is shown that this type of discretization enhances the accuracy of the RK model significantly. The eighth order isotropic gradient operator takes the following form:

$$\vec{\nabla} f(x, y) = \left[ \frac{\partial}{\partial x}, \frac{\partial}{\partial y} \right] f(x, y) \approx \sum_{i=1}^{25} \xi_i [d_i^x, d_i^y] f(x + d_i^x, y + d_i^y) \quad (24)$$

with

$$\begin{aligned} \xi &= [0, 960, 448, 960, 448, 960, 448, 960, 448, 84, \\ &\quad 32, 1, 32, 84, 32, 1, 32, 84, 32, 1, 32, 84, 32, 1, 32] / 5040 \\ \vec{d}^x &= [0, 0, 1, 1, 1, 0, -1, -1, -1, 0, 1, 2, 2, 2, 2, 1, \\ &\quad 0, -1, -2, -2, -2, -2, -2, -1] \\ \vec{d}^y &= [0, 1, 1, 0, -1, -1, -1, 0, 1, 2, 2, 2, 1, 0, -1, -2, \\ &\quad -2, -2, -2, -2, -1, 0, 1, 2, 2] \end{aligned} \quad (25)$$

Note that the previous operator assumes a unit lattice spacing in the  $x$  and  $y$  directions.

### 2.5. Setting the surface tension

Following a theoretical development by Reis and Phillips [9] and his predecessors [21], it is possible to predict the surface tension between the two fluids using only the basic parameters of the model. As in Refs. [9,13], knowing the form of the expression describing the surface tension and performing simulations on planar interfaces, a function of the model parameters can be determined to approximately describe the surface tension across an interface. It is very important to realize that the appropriate setting of the surface tension depends on the form of the color gradient and the discretization of the gradient operator.

For the isotropic color gradient discretization defined in Ref. [13] and in Eq. (14), the surface tension is set as follows [14]:

$$\sigma_{kl} = \frac{2}{9} \frac{\rho_k^0 + \rho_l^0}{\omega} (A_{kl} + A_{lk}) = \frac{2}{9} \frac{(1 + \frac{1}{\gamma_{kl}}) \frac{\rho_k^0}{2}}{\omega} (A_{kl} + A_{lk}) \quad (26)$$

In previous studies [9,14,13], the different values for  $\sigma_{kl}$  were set at the beginning of a simulation. Then, the parameters  $A_{kl} = A_{lk}$  were simulation constants calculated from the initial values of  $\rho_k$ ,  $\sigma_{kl}$  and  $\omega$ . Note that when the surface tension was not zero in these studies, the parameter  $\omega$  was a constant.

For isotropic color gradients defined as in Eq. (18), the surface tension is set as follows:

$$\sigma_{kl} = \frac{1}{9} \frac{(A_{kl} + A_{lk})}{\omega_{\text{eff}}} \quad (27)$$

The main difference between Eqs. (26) and (27) is that the color gradient in Eq. (18) is normalized by the total density. The different values for  $\sigma_{kl}$  are also set at the beginning of a simulation. However, the values for  $A_{kl} = A_{lk}$  are space- and time-dependent, because, in this study,  $\omega_{\text{eff}}$  may depend on space and time. So, the value for  $q$  in Eq. (13) is a new input parameter that needs to be properly selected when variable viscosity ratios are simulated.

## 2.6. Adjustment of the interface width for static contact angles

For three-phase flows and when the surface tension yields a Neumann triangle, as shown in Fig. (1), there is a possible equilibrium state where static contact angles  $\theta_{kl}$  will be formed between the fluids. Here, we follow the idea of Spencer et al. [18], who have found and demonstrated theoretically that a particular relation for  $\beta_{kl}$  at the triple fluid junction must be used, otherwise the angle  $\theta_{kl}$  will not be satisfied at steady state. This is more noticeable when one of the angles,  $\theta_{kl}$ , shown in Fig. (1), is small. The value of the angle  $\theta_{kl}$  can be found from the surface tension  $\sigma_{kl}$  using the law of cosines. By setting  $\theta_{\text{max}}$  as the largest  $\theta_{kl}$  in Fig. (1), the special relation for  $\beta_{kl}$  is:

$$\beta_{kl} = \begin{cases} \beta^0, & \text{kl with } \theta_{\text{max}} \\ \beta^0 (1 + c_{\text{triple}} (\sin(\pi - \theta_{\text{max}} - \theta_{kl}) - 1)), & \text{otherwise} \end{cases} \quad (28)$$

where  $\beta^0$  is a constant between 0 and 1 controlling the overall thickness of all three interfaces and

$$c_{\text{triple}} = \min \left\{ \eta_2 \frac{\rho_r \rho_g \rho_b}{\rho^3}, 1 \right\} \quad (29)$$

is a function that also varies between 0 and 1. It should be noted that the function  $c_{\text{triple}}$  is very similar to the one provided by Spencer et al. [18]. However, in [18], the threshold  $\eta_2 = 27$  and the “min” function are absent. In the setting of Spencer et al.,  $c_{\text{triple}}$  does not really reach unit value, and is usually less than 0.95. This cause some inaccuracy when one of the  $\theta_{kl}$  angles is small, i.e. the interface thickness ratio at the interface is not respected. In order to obtain the correct interface thickness ratio,  $c_{\text{triple}} = 1$  must be ensured for a certain number of sites at the triple fluid junction. This is why we used the free threshold parameter  $\eta_2 = 35$ , along with the “min” function. Therefore, the special form of the function  $c_{\text{triple}}$  makes it possible to fully activate the special relation for  $\beta_{kl}$  only at the triple fluid junction and for a reasonable number of lattice sites.

It is important to mention that, when there is no Neumann triangle, no relation for  $\beta_{kl}$  is known regarding the dynamic contact angles. The behavior of these contact angles is an active research topic in the LB community [25,26]. So, in this study, when there is no Neumann triangle, we merely set each of the  $\beta_{kl}$  to the same constant.

It can also be noted that, when the  $\theta_{kl}$  angles are close to 60 degrees, i.e. an equilateral Neumann triangle, the setting of all  $\beta_{kl}$  to the same value does not really affect the solution, because  $\sin(60) \approx 0.866$ , which is close to 1 [18].

Moreover, generalizing these relations is not straightforward when more than four fluids are in contact. One possibility, which is not easy to implement, would be to use only the three fluids most in evidence at each lattice site, and compute  $c_{\text{triple}}$  for these three fluids if there is a Neumann triangle. Then, we could use the relation in Eq. (28) for these three interfaces and set  $\beta_{kl} = \beta^0$  for the other interfaces. This would be equivalent to neglecting the effect of some fluids, and may not always work well, but would yield a reasonable approximation for some applications.

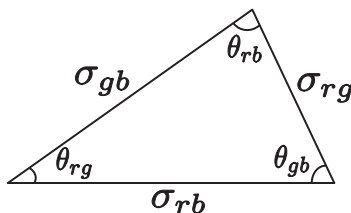


Fig. 1. Neumann's Triangle.



### 3. Numerical simulation

In this work, the figures showing multiphase flow are RGB images of size  $N_x \times N_y \times 3$  given by:

$$RGB = \frac{\begin{bmatrix} \rho_r \\ \rho_g \\ \rho_b \end{bmatrix}}{\sum_k \frac{\rho_k}{\rho_k^0}} \quad (30)$$

where  $N_x$  and  $N_y$  denote the number of lattice sites in the horizontal and vertical direction.

#### 3.1. Multiphase spinodal decomposition

Spinodal decomposition can be viewed as the physical process of phase separation of an emulsion. Here, we study the spinodal decomposition of an initial and random multiphase mixture. This is a very good numerical experiment in which to test the stability of the current LB model, and, in any case, any immiscible multicomponent model must pass the spinodal decomposition test. Although the results in this section are qualitative, they make it possible to test the robustness of the numerical code and see how the various fluids aggregate. A quantitative study of spinodal decomposition involving an RK model can be found in the work of Alexander et al. [27].

The setup is as follows. The computational domain is discretized with a lattice of  $N_x = 64$  by  $N_y = 64$  sites. Initially, for each site and with three fluid colors available (red, green, and blue), a uniform probability distribution is used to select a fluid color. Then, the site is filled with that fluid color using zero velocity equilibrium distribution functions. For the other fluids, the site is filled with zero density and velocity equilibrium distribution functions. The initial mixture is depicted in Fig. (2). Periodic boundary conditions are used at the four ends of the computational domain.

Three simulations were performed: Case I with a unit density and viscosity ratio, Case II with a high density and unit viscosity ratio, and Case III with a high density ratio and a high viscosity ratio. The simulation results are shown in Figs. 3–5 respectively. The results show that the algorithm is stable, and that spinodal decomposition is effectively taking place. Note that the unsteady behavior of the flow varies greatly, depending on the density and/or viscosity ratios. Also, with  $\alpha_k = 4/9$  ( $\kappa$  is the index of the least dense fluid) and  $\beta_{kl} = 0.5$ , the properties of the other fluids used are shown in Table (1). From the discussion in Section (2.6) on the adjustment of the interface width for static contact angles, since  $\beta_{kl}$  is the same for every interface, the contact angles at  $t = 1000000$  in Figs. 3–5 are about 60 degrees. This is a quantitative behavior that is theoretically expected. It is no surprise that the 60 degree angle is more accurate in the case of unit density ratios than in the other cases. In the section on the Laplace–Young law (3.4), the static contact angles are studied quantitatively in greater detail.

#### 3.2. Multilayered planar interfaces

The goal in this section is to test the model's ability to accurately simulate surface tension across different fluid interfaces. In theory, surface tension is independent of fluid viscosity. However, in this model, to set a specific surface tension between two fluids by means of Eq. (27), the fluid viscosity has to be taken into account, because the relaxation factor  $\omega_{\text{eff}}$  depends on it. In previous investigations [9,14,13], the correctness of the surface tension across a planar interface was only conducted for unit viscosity ratios and not verified for variable viscosity ratios between the interfaces. We will now address this issue, to show that the model accurately simulates surface tension, i.e. Eq. (27) is working properly, when there are both density and viscosity ratios across a planar interface.

The easiest way to test the multilayered planar interfaces is with the following flow configuration, as shown in Fig. (6). The variable  $x_k$  is used to note the different interface position between the fluids. The flow must be considered to be periodic in the x-axis, i.e.  $x_0$  and  $x_N$  are physically in the same fluid line.

The mechanical surface tension  $\sigma_{\text{mec}}$  is defined or studied, or both, in Refs. [2,28,21,9] for different flow configurations. Here, in the context of the previous specific flow setting,  $\sigma_{\text{mec}}$  takes the following form:

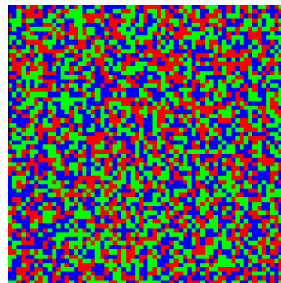


**Fig. 2.** Initial mixture for the spinodal decomposition simulation ( $t = 0$ ). (For interpretation of the references to color in this figure, the reader is referred to the web version of this article.)



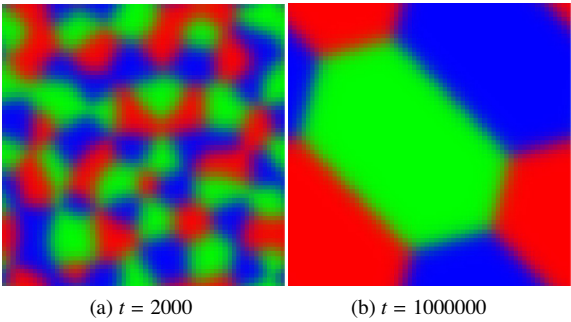


**Fig. 3.** Spinodal decomposition with *unit* density and *unit* viscosity ratios. (For interpretation of the references to color in this figure, the reader is referred to the web version of this article.)

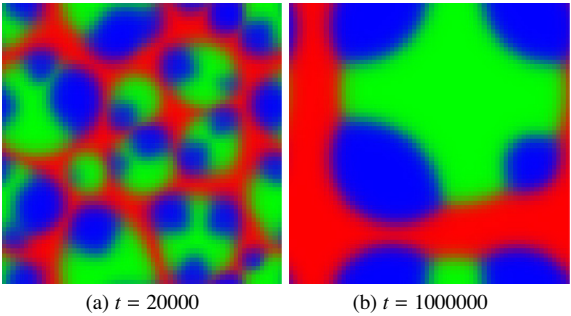


**Fig. 4.** Spinodal decomposition with *high* density and *unit* viscosity ratios. (For interpretation of the references to color in this figure, the reader is referred to the web version of this article.)

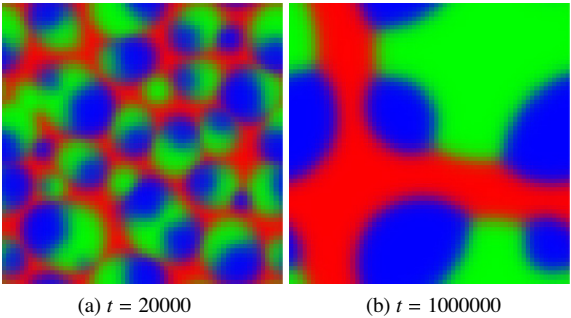


**Fig. 5.** Spinodal decomposition with *high* density and *high* viscosity ratios. (For interpretation of the references to color in this figure, the reader is referred to the web version of this article.)

**Table 1**  
Input parameters for the multiphase spinodal decomposition tests.

Parameters	Case I	Case II	Case III
$\rho_r$	1	100	100
$\rho_g$	1	10	10
$\rho_b$	1	1	1
$v_r$	1/6	1/6	1
$v_g$	1/6	1/6	1/10
$v_b$	1/6	1/6	1/100
$\sigma_{kl}$	$10^{-1}$	$10^{-1}$	$10^{-1}$
$q$	N/A	N/A	1

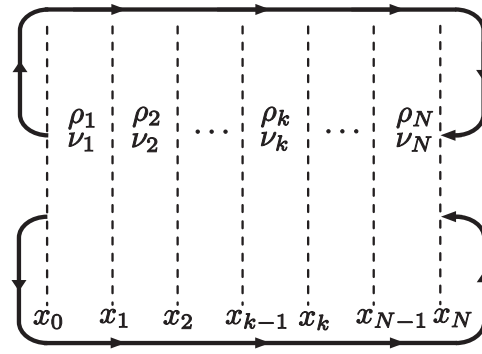


Fig. 6. Multilayered planar interface flow configuration.

$$\sigma_{\text{mec}} = \int_{x_0}^{x_N} (P_n(x) - P_t(x)) dx \quad (31)$$

where  $P_n$  and  $P_t$  are the normal and tangential components of the pressure tensor. The  $x$ -axis is a line of integration perpendicular to the interface. By setting  $\varphi_i^x$  as the relative angle between the  $x$ -axis and the vector  $\vec{c}_i$ , the components  $P_n$  and  $P_t$  are given by [9]:

$$\begin{aligned} P_n &= \sum_i N_i (|\vec{c}_i| \cos(\varphi_i^x))^2 \\ P_t &= \sum_i N_i (|\vec{c}_i| \sin(\varphi_i^x))^2 \end{aligned} \quad (32)$$

The setting of this test is described in the context of an LB simulation. First, only three layers of fluids,  $N = 3$ , are considered. The red fluid is on the left-hand side, the green fluid is in the middle, and the blue fluid is on the right-hand side. Since the mechanical surface tension is integrated along the  $x$ -axis and must take into account the surface tension of each fluid–fluid interfaces, we can conclude that the following relation must hold:

$$\sigma_{\text{mec}} = \sigma_{rg} + \sigma_{gb} + \sigma_{br} \quad (33)$$

The analytical flow solution for the surface tension is 1D, therefore a lattice containing  $90 \times 1$  sites is used and is geometrically located over the interval  $[x_0, x_N] = [0, 89]$ . Each fluid section is initialized with the zero velocity equilibrium distribution functions and is 30 sites wide. All fluid layers are 30 lattice units wide. The interfaces  $x_k$  are located between the fluid lattice sites. Periodic boundary conditions are applied in all four directions. The values  $\alpha_\kappa = 4/9$  ( $\kappa$  is the index of the least dense fluid) and  $\beta_{kl} = 1$  are used. For all multilayered planar interface simulations, the stopping criterion is the same, and is:

$$\frac{\sigma_{\text{mec}}^n - \sigma_{\text{mec}}^{n-2000}}{\sigma_{\text{mec}}^n} < 10^{-6} \quad (34)$$

with  $n$  the time step number. This check is only performed at every 2000 time steps.

A total of 192 numerical simulations were conducted to study how the various parameters in the current model influence the surface tension. The total number of all possible combinations of input parameters is  $192(4 \times 3 \times 2 \times 1 \times 2 \times 2 \times 1 \times 2)$ , as summarized in Table 2. The values for the surface tension must be of the same order, e.g.  $\sigma_{rg} = \sigma_{gb} = \sigma_{br} = \sigma$ , otherwise the computed value for  $\sigma_{rg} + \sigma_{gb} + \sigma_{br}$  will not represent each surface tension individually.

The initial condition for this problem can lead to instability, because the color-blind density distribution,  $N_1$ , and/or the fluid densities  $\rho_k$ , are initially discontinuous. It is then preferable to initialize the flow with a more continuous function. One way of doing this is described by Mei et al. [29], and is applied here in the context of multiphase flow. It consists in solving the model equation for a certain number of time steps with  $A_{kl} = 0$ , while imposing  $\vec{u} = 0$  in the equilibrium density

Table 2

Some combinations of parameters for the multilayered planar interface simulations.

$\vec{v} _q$	$\sigma$	$v_r$	$v_g$	$v_b$	$\rho_r$	$\rho_g$	$\rho_b$
$q = -1$	$10^{-5}$	1/2	1/6	1/6	30	1	1
$q = 0$	$10^{-3}$	1/6		1/100	1		1/30
$q = 1$	$10^{-1}$						
$q = 2$							

distribution in Eq. (7). So, for the simulations presented here, the first 2000 time steps only serve to stabilize the density distribution to a more continuous function.

Let us define the index  $j$  corresponding to the  $j^{\text{th}}$  simulation. The error for the  $j^{\text{th}}$  simulation is defined as follows:

$$E_j = \frac{|\sigma_{rg}^j + \sigma_{gb}^j + \sigma_{br}^j - \sigma_{mec}^j|}{\sigma_{mec}^j} \quad (35)$$

Tables (3) and (4) show the percentage error based on various norms applied over different simulation groups. More precisely, Table (3) displays the error as a function of the surface tension, while Table (4) shows the error when the following are considered: (i) only unit density and unit viscosity ratios; (ii) only non unit density and unit viscosity ratios; (iii) only unit density and non unit viscosity; and (iv) only non unit density and non unit viscosity ratios. The symbol  $\langle \cdot \rangle$  stands for the average.

From Table (3), it can be concluded for this simple test case that, whatever the viscosity  $q$ -average interpolation, the higher the surface tension, the greater is the relative accuracy of the model.

From Table (4), all the viscosity  $q$ -average interpolations seem to lead to similar accuracy, except for one case. Indeed, when simulating non unit density and viscosity ratios and small surface tension, the harmonic average, i.e. with  $q = -1$ , for interpolating viscosity leads to large inaccuracies.

For this test case, even if the accuracy is similar, we can still see from Table (3) and (4) that  $q = 2$  provides better results, then the accuracy decreases as  $q$  decreases.

To conclude, a careful analysis of the results will reveal that, based on our input parameters in Table (1), the multilayered planar interface is accurately simulated with errors under 2% for density ratios up to  $O(900)$  and viscosity ratios up to  $O(50)$  when using  $q = 1$  or 2. Note that we used the parameter  $\beta_{kl} = 1$  here. Now,  $\beta_{kl}$  can be lowered to obtain a larger interface, which would lead to a reduction in computational error and/or spurious current, and so improve stability. In the next two sections, we simultaneously obtain stable and accurate simulations with high density and viscosity ratios of up to  $O(1000)$  and  $O(100)$  respectively by lowering  $\beta_{kl}$  to 0.5.

### 3.3. Multiphase Laplace law

The next numerical experiment involves the evolution of a three-phase flow, where the steady state solution corresponds to a similar setup of a Laplace law numerical experiment [14]. This test is used to assess the ability of the model to perform an unsteady simulation, where the qualitative behavior of the flow evolution can be predicted. Moreover, a final steady state solution exists on which we can measure and predict the final surface tension. Note that this section is presented primarily to show that the generalization of the model from two phases to  $N$  phases does not break Laplace's law.

**Table 3**

Errors in percentage (%) based on various norms, simulations sets, and effective relaxation factors for the multilayered planar interfaces.

Simulations sets $\{E_j [\cdot]\}$					
	$\{E_j \sigma_{kl} = 10^{-5}\}$	$\{E_j \sigma_{kl} = 10^{-3}\}$	$\{E_j \sigma_{kl} = 10^{-1}\}$		$\bar{v} _q$
$\max\{\cdot\}$	3.961e + 01	2.063e + 00	1.501e + 00	$q = -1$	
	4.469e + 00	1.712e + 00	1.693e + 00	$q = 0$	
	1.122e + 00	8.442e-01	8.442e-01	$q = 1$	
	1.427e + 00	1.670e-01	1.672e-01	$q = 2$	
$\langle\{\cdot\}\rangle$	3.706e + 00	7.712e-01	7.297e-01	$q = -1$	
	9.807e-01	6.937e-01	6.906e-01	$q = 0$	
	4.111e-01	3.350e-01	3.351e-01	$q = 1$	
	2.411e-01	5.422e-02	5.263e-02	$q = 2$	

**Table 4**

Errors in percentage (%) based on various norms, simulations sets, and effective relaxation factors for multilayered planar interfaces.

Simulations sets $\{E_j [\cdot]\}$					
	$[\rho_k = 1, \nu_k = 1/6]$	$[\nu_k = 1/6, \exists k : \rho_k \neq 1]$	$[\rho_k = 1/6, \exists k : \nu_k \neq 1]$	$[\exists k : \nu_k \neq 1/6, \exists k : \rho_k \neq 1]$	$\bar{v} _q$
$\max\{\cdot\}$	1.430e-03	1.587e-01	1.501e + 00	3.961e + 01	$q = -1$
	1.430e-03	1.587e-01	1.693e + 00	4.469e + 00	$q = 0$
	1.430e-03	1.587e-01	8.442e-01	1.122e + 00	$q = 1$
	1.430e-03	1.587e-01	4.549e-02	1.427e + 00	$q = 2$
$\langle\{\cdot\}\rangle$	1.430e-03	6.001e-02	9.918e-01	2.735e + 00	$q = -1$
	1.430e-03	6.001e-02	9.488e-01	1.065e + 00	$q = 0$
	1.430e-03	6.001e-02	4.745e-01	4.624e-01	$q = 1$
	1.430e-03	6.001e-02	3.187e-02	1.754e-01	$q = 2$

The setup is as follows. A lattice of  $128 \times 128$  sites is used with periodic boundary conditions at the four ends. The computational domain then measures 127 lattice units in both height and width. The corner at the bottom left of the domain is located at the origin  $(0, 0)$ . The fluids are initialized using the zero velocity equilibrium distribution functions. The red fluid is initialized at the following position:

$$(x - 63.5)^2 + (y - 73.5)^2 \leq 30^2 \text{ and } y > 73.5 \quad (36)$$

$$(x - 63.5)^2 + (y - 53.5)^2 \leq 30^2 \text{ and } y < 53.5 \quad (37)$$

The green fluid is initialized at the following position:

$$33.5 < x < 93.5 \text{ and } 53.5 < y < 73.5 \quad (38)$$

The remaining lattice sites are filled with blue fluid. Fig. (7a) shows the initial condition of this setup. A numerical simulation is performed for each of the three cases, I, II, and III. The input parameters for these simulations are presented in Table (5).

As described in Section (3.2), the initial condition of this problem can lead to instability. Therefore, the first 2000 time steps are used to stabilize that condition.

By adding the surface tension forces at the initial triple junction point of the fluids, we can see that, because the flow is initially at rest and  $\sigma_{gb}$  is significantly larger than the sum of the other two surface tension forces, the red fluid will start to encircle the green fluid. In fact, it will completely surround the green fluid, and the green–blue interface will disappear. Because  $\sigma_{rg}$  and  $\sigma_{rb}$  are non zero, in the long run, the steady state solution is a green circular bubble inside a red circular annulus, the outside of which is surrounded by blue fluid. The numerical solution at steady state and at intermediate times is presented in Fig. (7) for case III with a high density and a high viscosity ratio. It should be noted that case I with unit density ratio is similar. Moreover, the qualitative behavior of the flow agrees well with the previously expected scenario.

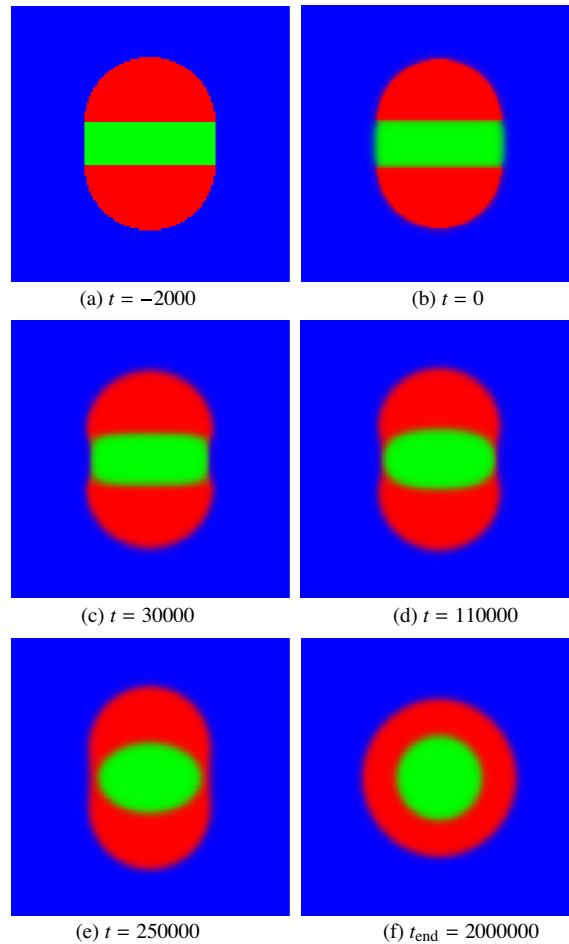


**Fig. 7.** Unsteady flow converging to a steady state three phase flow configuration. (For interpretation of the references to color in this figure, the reader is referred to the web version of this article.)

**Table 5**

Input parameters for the three phase flow Laplace law tests.

Parameters	Case I	Case II	Case III
$\beta_{kl}$	0.7	0.7	0.5
$\alpha_b$	4/9	4/9	4/9
$\rho_r$	1	1000	1000
$\rho_g$	1	$\sqrt{1000}$	$\sqrt{1000}$
$\rho_b$	1	1	1
$v_r$	1/6	1/6	1
$v_g$	1/6	1/6	1/10
$v_b$	1/6	1/6	1/100
$\sigma_{rg}$	8e-02	8e-02	8e-02
$\sigma_{rb}$	8e-02	8e-02	8e-02
$\sigma_{gb}$	4e-01	4e-01	4e-01
$q$	N/A	N/A	1

At steady state, if the Laplace law for two-phase flow is applied iteratively across the two interfaces  $r$ - $g$  and  $r$ - $b$ , we should obtain the following result:

$$\sigma_{rg} + \sigma_{rb} = \Delta P_{gr} R_g + \Delta P_{rb} R_r \quad (39)$$

where  $\Delta P_{gr} = P_g - P_r$  and  $\Delta P_{rb} = P_r - P_b$  indicate the pressure jumps across the various fluid interfaces. Also,  $R_g$  is the radius of the green circular bubble and  $R_r$  is the outer radius of the red fluid annulus.

Here, the average pressure inside the fluid section of color  $j$  is measured as the sum of the local average pressure of each fluid  $k$ , as follows:

$$P_j = \sum_k \frac{3 \langle \rho_{kj} \rangle (1 - \alpha_k)}{5} \quad (40)$$

with  $\langle \rho_{kj} \rangle = \langle \{ \rho_k | \rho_j^0 \rho_j \geq 0.99 \} \rangle$ . The symbol  $\langle \cdot \rangle$  stands for the average. There are 2828 red and 1200 green sites initially, and, because of the incompressible limit of the LB model, the radii  $R_g$  and  $R_r$  can be estimated to be equal to  $\sqrt{1200/\pi}$  and  $\sqrt{(1200 + 2828)/\pi}$  respectively.

For each parameter case, I, II, and III, Table (6) shows the relative percentage errors with Eq. (39) obtained at steady state for different concentration factors, i.e. Eqs. (21) or (22). The left-hand side of Eq. (39) is used as the reference to calculate the relative errors. The model greatly underestimates the surface tension when using Eq. (22) instead of Eq. (21).

Note that the numerical steady state in Case I and Case II is regarded as achieved when:

$$\max_{\text{all sites}} \left\{ \left| \frac{(N_i)^{(n)} - (N_i)^{(n-1)}}{(N_i)^{(n)}} \right| \right\} \leq \epsilon \quad (41)$$

with  $\epsilon = 10^{-7}$ , while  $n$  denotes the time step number. To reduce the computational cost, this condition is only checked every 2000 time steps. Note that in Case III, with both high density and high viscosity ratios, numerical noise is present and prevents the simulation from converging with such a restrictive numerical steady state condition. This might be related to the fact that the numerical scheme is at the limit of numerical stability. So, for Case III, the simulations were stopped after 2000000 time steps.

Fortunately, with the current model and for this test case, the relative errors for the three phase Laplace law are acceptable, even with high density and high viscosity ratios up to  $O(1000)$  and  $O(100)$  respectively. The large discrepancies obtained with the concentration factor in Eq. (22) show that it is very important for the numerical method to be carefully designed so that the generalization to  $N$ -phase flow does not break Laplace's law. Here, we do not repeat further results concerning Laplace's law, as this has been extensively studied in [14].

It is important to note that we do not think that the concentration factor in Eq. (22) is incorrect, but, by choosing that concentration factor, another multiplicative constant ( $\neq 1/9$ ) would need to be chosen in Eq. (27) for the definition of the surface tension. It appears to us much more difficult to find a multiplicative constant that works well for a wide range

**Table 6**

Relative errors for the three phase flow Laplace law tests.

$C_{kl}$	Case I	Case II	Case III
Eq. (21)	0.734%	2.831%	4.034%
Eq. (22)	54.17%	52.24%	53.29%

of parameters. With the concentration factor in Eq. (22), this multiplicative constant could be determined using a planar interface simulation prior to any more complex simulations, but it would be a heuristic determination and would not work in the case of a simulation with variable surface tension.

In order to correctly simulate the unsteady multiphase flow converging to the Laplace law setup, two choices were carefully made. First, an appropriate definition of the concentration factor, i.e. Eq. (21), and second, a suitable definition of the color gradient, i.e. Eq. (18).

### 3.3.1. Appropriate choice of the color gradient

In this section, we show numerically why the choice of color gradient is important when generalizing the model from two to  $N$  phases. With the same setting as with Case II in Section (3.3), except that  $\sigma_{rg} = \sigma_{rb} = 8e - 05$  and  $\sigma_{gb} = 4e - 04$ , Fig. (8) shows the results obtained for  $\rho_r$ ,  $\rho_g$ , and  $\rho_b$ , depending on the choice of color gradient, i.e. Eq. (15) or Eq. (18). The online version of Fig. (8) may provides a better understanding. Paying careful attention to the images, it becomes clear that there is a non physical mass flow leak in the direction tangential to the interfaces when the color gradient  $\vec{F}_{kl}^{natural}$  is use. This false phenomenon is obviously undesired, and, depending on the setting of a simulation, may easily spoil the results. We have not yet investigated why this is so. Fortunately, when using  $\vec{F}_{kl}$  in Eq. (18), this non physical behavior does not occur.

### 3.4. Laplace-Young's law

The goal in this section is to verify whether or not the model can correctly simulate the static contact angles at a triple fluid junction as a function of the surface tension. In the current study, this numerical test is the only one that really checks the quantitative behavior of the model for a flow with three phases. It will then be numerically investigated and described in detail. A complementary goal is to define a simple and robust quality index to measure the accuracy of any LB model with respect to the static contact angles. Before going into the details of this test, we wish to point out that Refs. [20,18] have addressed the subject of contact angles with three phases within the LB framework. This study has also been conducted in Refs. [30,31] using other numerical methods.

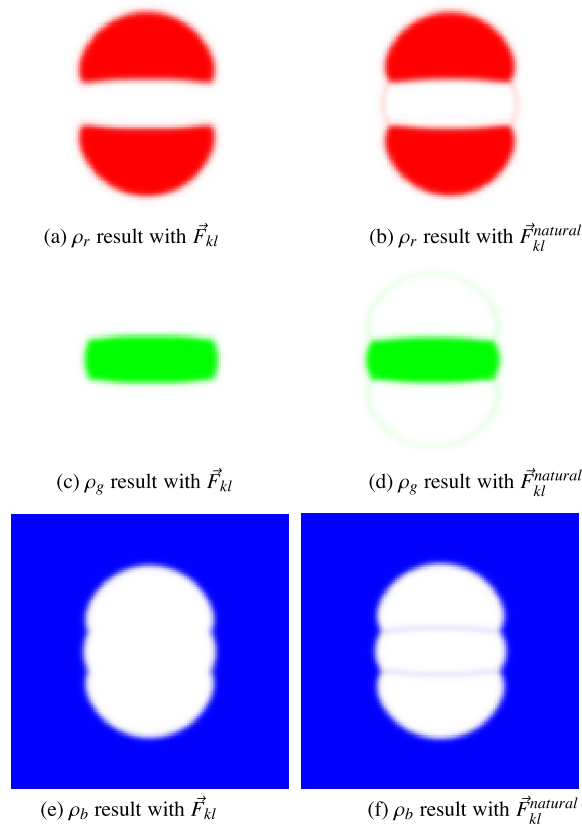


**Fig. 8.** Mass flow leakage in the direction tangential to the interface at  $t = 8000$ . (For interpretation of the references to color in this figure, the reader is referred to the web version of this article.)

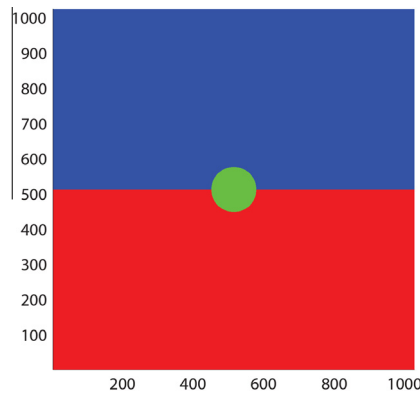


**Fig. 9.** Typical initial condition for a Laplace–Young law simulation. (For interpretation of the references to color in this figure, the reader is referred to the web version of this article.)

We now discuss the flow configuration in the context of an LB setting. A lattice of  $N_x \times N_y$  sites is used with periodic boundary conditions at the four ends. The corner at the bottom left of the domain is located at the origin  $(0, 0)$ . The fluids are initialized using the zero velocity equilibrium distribution functions. The green fluid is initialized at the following position:

$$\left(x - \left(\frac{N_x - 1}{2}\right)\right)^2 + \left(y - \left(\frac{N_y - 1}{2}\right)\right)^2 \leq \left(\frac{N_x}{2}\right)^2 \quad (42)$$

The red fluid is initialized at the remaining sites available in the section  $y < \frac{N_y - 1}{2}$ . The other lattice sites are filled with blue fluid. Fig. (9) shows the initial conditions of this setup for  $N_x = 1024$  and  $N_y = 1024$ . The green bubble may appear small when compared to the computational domain, but its size has been chosen to accommodate the simulations with very small contact angles. Also, the green bubble is small, in order to avoid the perturbation coming from the periodic boundary conditions. As described in Section (3.2), the initial condition of this problem can lead to instability. Therefore, the first 2000 time steps are used to stabilize the initial condition.

The stopping criterion for all simulations is a dynamic procedure which combines two criteria. Let us denote  $n$  the time step number and  $Q_{\text{old}}$ , updated every 2000 time steps, the last quality index of the simulation that is kept in the computer memory. First,  $|Q^n - Q_{\text{old}}| < 10^{-5}$  must be true for 50000 time steps in a row. If the previous condition is true, then  $|\frac{Q^n - Q_{\text{old}}}{Q^n}| < 10^{-5}$  is checked. If it is true, the simulation stops, if not, the counter, which is then at 50000, is reset to 0 and the simulation continues. As in Section (3.3), with both high density and high viscosity ratios, numerical noise is present and may prevents the simulation from converging with such a restrictive numerical steady state condition. So, in Table (9), the simulations (a) with lattice size  $128 \times 128$  and  $256 \times 256$  were stopped after 5000000 time steps. All the others simulations have converged correctly.

In all the simulations, the following parameters are constant:  $\sigma_{rb} = 10^{-2}$ , and  $\alpha_\kappa = 4/9$ . Three sets of simulations are considered:

1. One with unit density and viscosity ratios, i.e. with  $\rho_k = 1$ ,  $\nu_k = 1/6$ , and  $\beta_0 = 0.7$ .
2. One with high density ratios, but unit viscosity ratios, i.e. with  $\rho_r = 1$ ,  $\rho_g = 1000$ ,  $\rho_b = 1$ ,  $\nu_k = 1/6$ , and  $\beta_0 = 0.7$ .
3. One with both high density and high viscosity ratios, i.e. with  $\rho_r = 1$ ,  $\rho_g = 1000$ ,  $\rho_b = 1$ ,  $\nu_r = 1/100$ ,  $\nu_g = 1$ ,  $\nu_b = 1/100$ , and  $\beta_0 = 0.5$ .

For each simulation set, the surface tensions  $\sigma_{rg}$  and  $\sigma_{gb}$  are varied, in order to generate different contact angles,  $\theta_{rg}$  and  $\theta_{gb}$ . Tables 7–9 show the missing parameters and the results of these simulations.

At steady state, the expected flow configuration is shown in Fig. (10) when a Neumann triangle exists. This is deduced from Laplace–Young’s law. Based on geometric considerations, we can define the following variables:

**Table 7**

Quality index and order of convergence for different static contact angles with unit density ratios.

	Unit density ratios				Quality index: $Q$				Order	$Q_{512}/Q_{1024}$
	$\sigma_{rg} \cdot 10^2$	$\sigma_{gb} \cdot 10^2$	$\theta_{rg}$	$\theta_{gb}$	128x128	256x256	512x512	1024x1024		
(a)	1.40	0.60	120.0	21.79	1.44e–01	9.20e–02	5.62e–02	2.93e–02	0.760	1.921
(b)	1.40	1.40	69.08	69.08	1.40e–01	6.80e–02	3.47e–02	1.79e–02	0.986	1.937

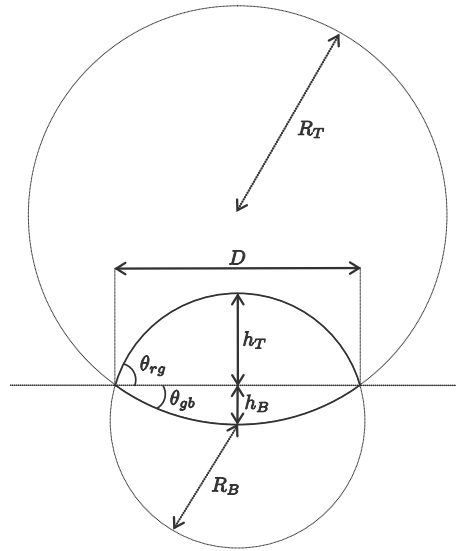


**Table 8**Quality index and order of convergence for different static contact angles with *high density ratios*.

	High density ratios				Quality index: $Q$				Order	$Q_{512}/Q_{1024}$
	$\sigma_{rg} \cdot 10^2$	$\sigma_{gb} \cdot 10^2$	$\theta_{rg}$	$\theta_{gb}$	128x128	256x256	512x512	1024x1024		
(a)	1.40	0.60	120.0	21.79	2.60e-01	1.17e-01	5.57e-02	2.61e-02	1.101	2.130
(b)	1.40	1.40	69.08	69.08	1.24e-01	6.35e-02	3.20e-02	1.55e-02	0.998	2.066

**Table 9**Quality index and order of convergence for different static contact angles with *high density and high viscosity ratios*.

	High density and viscosity ratios				Quality index: $Q$				Order	$Q_{512}/Q_{1024}$
	$\sigma_{rg} \cdot 10^2$	$\sigma_{gb} \cdot 10^2$	$\theta_{rg}$	$\theta_{gb}$	128x128	256x256	512x512	1024x1024		
(a)	1.40	0.60	120.0	21.79	3.29e-01	1.56e-01	6.03e-02	2.56e-02	1.243	2.357
(b)	1.40	1.40	69.08	69.08	1.86e-01	9.26e-02	4.55e-02	2.34e-02	0.999	1.948

**Fig. 10.** Expected steady state configuration for the green fluid deduced from the Laplace–Young law.

$$D = 2 \sqrt{\frac{A_g}{\sum_{kl=rg,gb} \frac{1}{\sin(\theta_{kl})} \left( \frac{\theta_{kl}}{\sin(\theta_{kl})} - \cos(\theta_{kl}) \right)}} \quad (43)$$

$$h_T = \frac{D}{2} \left( \frac{1 - \cos(\theta_{rg})}{\sin(\theta_{rg})} \right) \quad (44)$$

$$h_B = \frac{D}{2} \left( \frac{1 - \cos(\theta_{gb})}{\sin(\theta_{gb})} \right) \quad (45)$$

$$L_i = \sqrt{h_i^2 + (D/2)^2}, \quad i = T, B \quad (46)$$

$$R_i = \frac{\left( \frac{L_i}{2} \right)^2}{\sqrt{1 - \left( \frac{D/2}{L_i} \right)^2}}, \quad i = T, B \quad (47)$$

$$\theta_i = 2 \arccos \left( \frac{R_i - h_i}{R_i} \right), \quad i = T, B \quad (48)$$

where  $A_g$  is the initial area of the green fluid. In our case,  $A_g$  equals the initial number of green sites. Following this, a *quasi-analytical solution*, i.e. two arc circles, for the position of the top and bottom interface can be found:

$$R_r e^{i\theta} + x_c + i(y_c - (R_r - h_r)), \quad +\pi - \theta_T \leq 2\theta \leq +\pi + \theta_T \quad (49)$$

$$R_b e^{i\theta} + x_c + i(y_c + (R_b - h_b)), \quad -\pi - \theta_B \leq 2\theta \leq -\pi + \theta_B \quad (50)$$

Note that  $i = \sqrt{-1}$  in the previous two arc circle equations, and that  $x_c = (N_x - 1)/2$ . We describe the above equations as a quasi-analytical solution, because the position of  $y_c$  is not known a priori when the simulation is started. This is because of the periodic boundary and initial conditions. For example, with variable density ratios and depending on the surface tension, a large amount of momentum is transferred between the various fluid colors and the position of  $y_c$  changes. Moreover, the final value of  $y_c$  is not known, which is why we describe it now. First, a set of  $y$  values is defined:

$$\{y_1, y_2, \dots, y_n, \dots, y_{16}\} = \{y \mid 16 \text{ sites with } \frac{\rho_r \rho_b \rho_g}{\rho^3} \text{ maximum}\} \quad (51)$$

Then, the value used for  $y_c$  is defined as:

$$y_c = \frac{\sum_{n=1}^{16} y_n \left( \frac{\rho_r \rho_b \rho_g}{\rho^3} \right)_n}{\sum_{n=1}^{16} \left( \frac{\rho_r \rho_b \rho_g}{\rho^3} \right)_n} \quad (52)$$

### 3.4.1. Laplace-Young's law: Quality index

From the quasi-analytical position of the interfaces, we can define the following quality index:

$$Q = \sqrt{\left( \frac{\rho_r^{\text{tot}} - \rho_r^{\text{out}}}{\rho_r^{\text{tot}}} \right)^2 + \left( \frac{\rho_b^{\text{tot}} - \rho_b^{\text{out}}}{\rho_b^{\text{tot}}} \right)^2 + \left( \frac{\rho_g^{\text{tot}} - \rho_g^{\text{in}}}{\rho_g^{\text{tot}}} \right)^2} \quad (54)$$

where  $\rho_k^{\text{tot}}$  is the total amount of  $k$  fluid in the computational domain. Also,  $\rho_k^{\text{out}}$  is the amount of  $k$  fluid that is outside the two quasi-analytical arc circles, while  $\rho_k^{\text{in}}$  is the amount of  $k$  fluid inside them. Note that  $Q = 0$  indicates *indirectly* that the interfaces between the fluids are located exactly where predicted by the analytical solution. Also, this quality index is easier to use, and is more robust and reliable than any heuristic method of calculating the contact angles numerically.

### 3.4.2. Laplace-Young's law: Results

Table (7) shows, for unit density ratios, the quality index  $Q$  obtained at steady state for different lattice sizes, ranging from  $128 \times 128$  to  $1024 \times 1024$ . Tables (8) and (9) show the same test, but for high density ratios and unit or high viscosity ratios.

The order of convergence of the quality index in terms of lattice size is also computed, and presented in Tables 7–9. The order of convergence is computed as the absolute value of the slope of the best fit line in a log–log scale of the quality index  $Q$  versus the lattice size  $N_x$ .

From these results, we can deduce that this LB model is compatible with the analytical solution of Laplace-Young's law, because the order of convergence of the quality index  $Q$  is about 1. Note that, where the order of convergence is much lower than 1, e.g. case (a) with a convergence order equal to 0.76 in Table (7), the value for  $Q_{512}/Q_{1024}$  equals 1.921 and is about 2, which confirms first order accuracy and indicates that the lattice would need to contain, for this case, more sites, in order to see the first order accuracy appear. For the high density ratios and the high viscosity ratio simulations, since  $\beta_0 = 0.5$  and so the interface fluids are thicker, the quality index  $Q$  for these simulations is higher, but the order of convergence is still about 1.

It is important to emphasize that LB models are usually thought to be second order accurate, but that is true for a single-phase flow and not necessarily for multiphase flows. From our knowledge, only the basic LB streaming combined with the BGK collision was shown to be second order accurate in time and space for the conserved variables  $\rho$  and  $\rho \bar{u}$ , and not with the multiphase collision operator. However, for simulating incompressible flows, it should be noted that the basic lattice Boltzmann method behaves like a first order method in time because of the compressibility error [32]. So it is no surprise that the scheme is first order in terms of the quality index. It is believed that LB models for simulating multiphase flow may only be first order accurate in space and time *at the interface* for the conserved variables  $\rho$  and  $\rho \bar{u}$ . Second order accuracy is only achieved in regions of a pure phase. Obtaining second order accuracy at the interface is difficult, because the combination of all the operators would need to be constructed in such a way as to satisfy, at the macroscopic level, the Navier-Stokes equations to second order. This appears to be difficult to achieve, but may be possible.

Even though the contact angles are small, the model still captures the correct contact angles. We recall that this is not possible, at least for this model, without the special relations in Eq. (28) for  $\beta_{kl}$ . Without these special formulas, the scheme simply becomes incompatible with the analytical solution. In other words, the order of convergence would rapidly decrease to zero as the lattice size increases. For example, when case (a), with unit density ratios from Table (7), was simulated by setting the coefficients to  $\beta_{kl} = \beta^0$  instead of using the special relations in Eq. (28), we found that the order of convergence for the quality index  $Q$  dropped to 0.635. Moreover,  $Q_{512}/Q_{1024} = 1.564$  for that case, so there was no sign of compatibility with the analytical solution using  $\beta_{kl} = \beta^0$ .

Fig. (11) shows the numerical solution of the simulations at steady state with the unit density ratios presented in Table (7). Figs. (12) and (13) show the same solutions, but with the simulations presented in Tables (8) and (9) with high den-

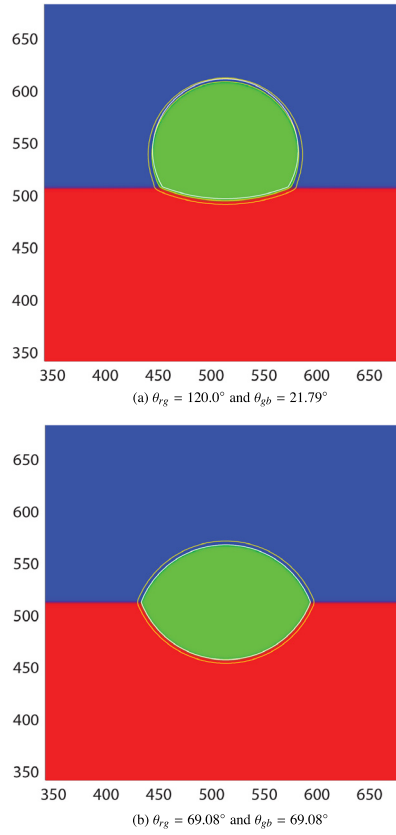


**Fig. 11.** Steady state solution at unit density and unit viscosity ratios for different contact angles. (For interpretation of the references to color in this figure, the reader is referred to the web version of this article.)

sity ratios and with unit/high viscosity ratios. The quasi analytical arc circles and the contours of the functions  $\rho_g/\rho_g^0 = 0.5$  and  $\rho_g/\rho_g^0 = 0.01$  are also plotted, in order to visualize the theoretical versus the numerical position of the interface. The two contour values give an idea of the interface width. These figures are provided to make it possible to visualize that the density and viscosity ratios have very little effect on the numerical steady state contact angles. Note that the axes were rescaled in order to emphasize the plot on the green bubble.

In concluding this section, we can infer that Laplace–Young’s law is correctly embedded in this model, i.e. the surface tension alone is enough to achieve the theoretical steady state contact angles between the fluids.

### 3.5. Multilayered Couette’s flow

The purpose of this numerical test is to investigate the model’s ability to simulate flow with variable dynamic viscosity. The multilayered Couette’s flow consists of multiple layers of fluids between two infinite moving plates, as shown in Fig. (14).

The variable  $x_k$  is used to denote the interface position between the fluids with properties  $(\rho_k, \mu_k)$  and  $(\rho_{k+1}, \mu_{k+1})$ , where  $\mu_k = \rho_k \nu_k$  is the dynamic viscosity. The walls located at positions  $x_0$  and  $x_N$  are moving vertically at a velocity of  $v_0^y$  and  $v_N^y$  respectively.

At steady state and applying the incompressibility hypothesis, an analytical solution exists for the previous flow setting (see Ref. [33] for the three-layer case). Here, we derive a generalized solution for the N phase Couette’s flow. From the Navier–Stokes equations, each fluid layer  $k$  should respect:

$$\frac{\partial^2}{\partial x^2} v_k^y = 0 \quad (55)$$

This leads to multiple linear velocity profiles within each interval  $x_{k-1} \leq x \leq x_k$ , of the form:

$$v_k^y = a_k x + b_k \quad (56)$$

Both boundary conditions and interface conditions must be provided to solve the partial differential equation problem. Physical considerations imply that the velocity in Eqs. (59) and the shear stress in Eqs. (60) must be continuous at each of the interfaces [34]. Therefore, the boundary conditions are:

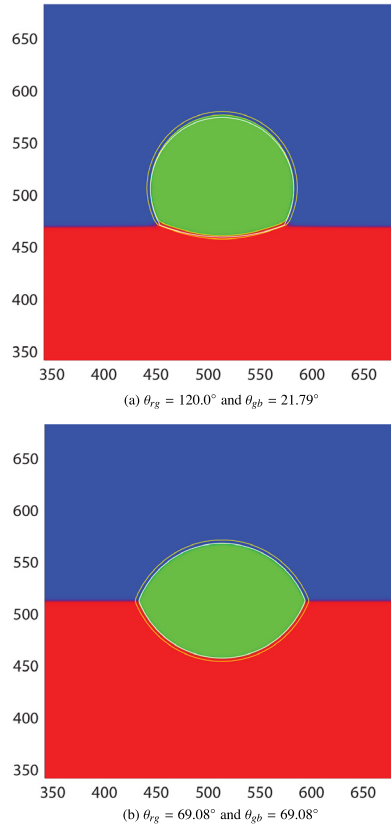


**Fig. 12.** Steady state solution at *high* density and *unit* viscosity ratios for different contact angles. (For interpretation of the references to color in this figure, the reader is referred to the web version of this article.)

$$v^y(x_0) = v_0^y \quad (57)$$

$$v^y(x_N) = v_N^y \quad (58)$$

and the interface conditions are:

$$v_k^y(x_k) = v_{k+1}^y(x_k) \quad (59)$$

$$\mu_k \frac{\partial v_k^y}{\partial x} \Big|_{x_k} = \mu_{k+1} \frac{\partial v_{k+1}^y}{\partial x} \Big|_{x_k} \quad (60)$$

In order to obtain the analytical solution, i.e. the coefficients  $a_k$  and  $b_k$ , a linear system can be written as:

$$\begin{pmatrix} x_0 & 1 & 0 & 0 & 0 & 0 & 0 & 0 & \dots & 0 & 0 \\ \vdots & \vdots & \vdots & \vdots & \vdots & \vdots & \vdots & \vdots & \vdots & \vdots & \vdots \\ \mathbf{C}_1 & & \mathbf{D}_1 & & 0 & 0 & 0 & 0 & \dots & 0 & 0 \\ \vdots & \vdots & \vdots & \vdots & 0 & 0 & 0 & 0 & \dots & 0 & 0 \\ 0 & 0 & \mathbf{C}_2 & & \mathbf{D}_2 & & 0 & 0 & \dots & 0 & 0 \\ \vdots & \vdots & \vdots & \vdots & \vdots & \vdots & \vdots & \vdots & \vdots & \vdots & \vdots \\ 0 & 0 & 0 & 0 & \ddots & \ddots & \ddots & \ddots & 0 & 0 & 0 \\ \vdots & \vdots & \vdots & \vdots & \vdots & \vdots & \vdots & \vdots & \vdots & \vdots & \vdots \\ 0 & 0 & 0 & 0 & 0 & 0 & 0 & 0 & \dots & 0 & 0 \\ \vdots & \vdots & \vdots & \vdots & \vdots & \vdots & \vdots & \vdots & \vdots & \vdots & \vdots \\ 0 & 0 & 0 & 0 & 0 & 0 & 0 & \mathbf{C}_{N-1} & & \mathbf{D}_{N-1} & \\ \vdots & \vdots & \vdots & \vdots & \vdots & \vdots & \vdots & \vdots & \vdots & \vdots & \vdots \\ 0 & 0 & 0 & 0 & 0 & 0 & 0 & 0 & 0 & x_N & 1 \end{pmatrix} \cdot \begin{pmatrix} -a_1 \\ b_1 \\ -a_2 \\ b_2 \\ -a_3 \\ \vdots \\ \vdots \\ b_{N-1} \\ -a_N \\ b_N \end{pmatrix} = \begin{pmatrix} -v_0^y \\ 0 \\ 0 \\ 0 \\ 0 \\ \vdots \\ \vdots \\ 0 \\ 0 \\ v_N^y \end{pmatrix} \quad (61)$$

with

$$\mathbf{C}_k = \begin{pmatrix} \mu_k & 0 \\ x_k & 1 \end{pmatrix} \quad (62)$$

and

$$\mathbf{D}_k = \begin{pmatrix} -\mu_{k+1} & 0 \\ -x_k & -1 \end{pmatrix} \quad (63)$$

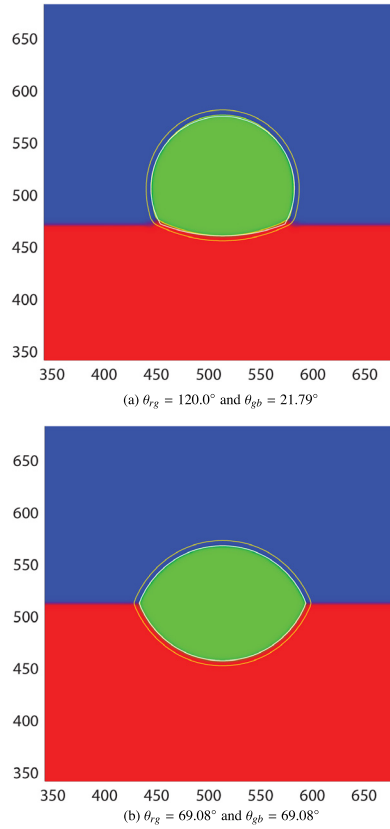


**Fig. 13.** Steady state solution at *high* density and *high* viscosity ratios for different contact angles. (For interpretation of the references to color in this figure, the reader is referred to the web version of this article.)

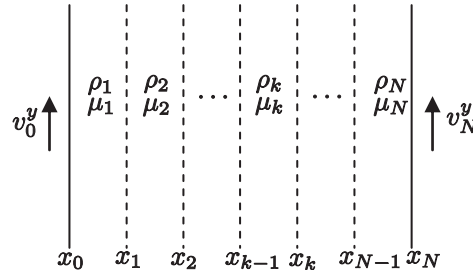


**Fig. 14.** Couette's flow configuration.

Now that the generalized analytical solution for the multilayered Couette's flow has been presented, the setting for this test is described in the context of an LB simulation. Only six layers of fluids,  $N = 6$ , are considered. Since the analytical solution is 1D, a lattice containing  $N_x = 90$  by  $N_y = 1$  sites is used, and is located over the interval  $[x_0, x_N] = [0, 89]$ . Each fluid section is initialized with the zero velocity equilibrium distribution functions, and is 15 sites wide. The first and last fluid layers are 14.5 lattice units wide, while the other layers are 15 lattice units wide. The wall located at  $x_0$  and  $x_N$  passes over the lattice sites, while the interfaces  $x_1$  to  $x_{N-1}$  pass between the fluid lattice sites. Because the model is 2D, periodic boundary conditions are applied in the  $y$ -direction. The first and last sites are located where the velocity boundary conditions are implemented. The standard Zou and He [35] velocity boundary condition is applied. The wall velocities are set to  $v_0^y = 0.01$  and  $v_N^y = 0$ . The stopping criterion, Eq. (41), is the same as that used in the multiphase Laplace law section, but with  $\epsilon = 10^{-10}$ . Values of  $\alpha_k = 4/9$  ( $k$  index of the least dense fluid) and  $\beta_{kl} = 1$  are used.

### 3.5.1. Multilayered Couette's flow with unit density ratios

The goal in this section is to show that the model can correctly simulate Couette's flow with variable kinematic viscosity between the fluid layers. It is also important to show that the choice of viscosity interpolation  $\bar{v}|_q$  can have a positive impact,

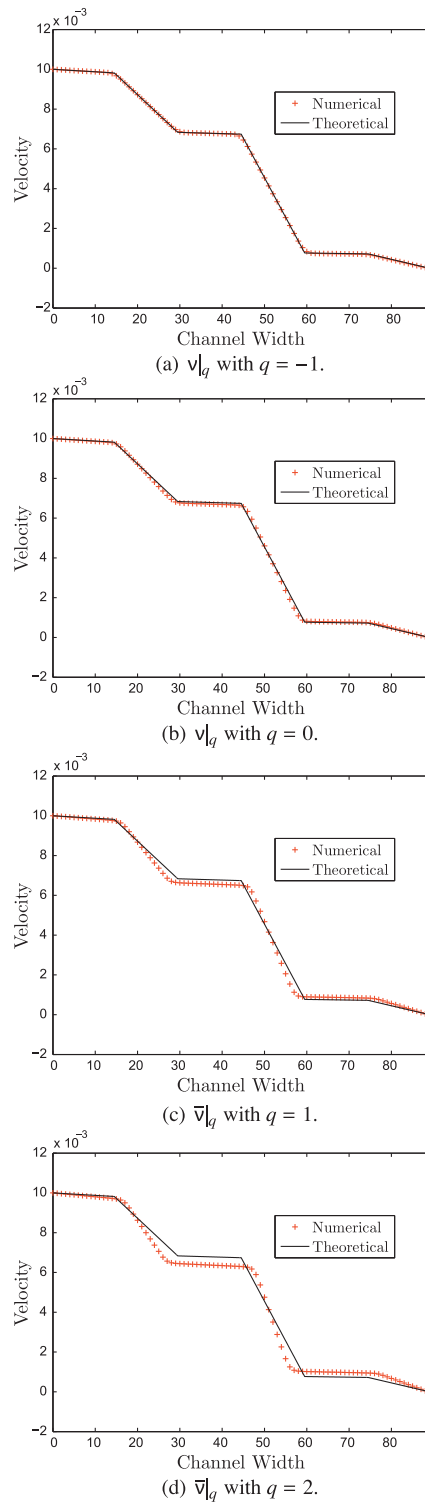


**Fig. 15.** Numerical and theoretical velocity profile for the multilayered Couette's flow with unit density ratios.

because the accuracy of the model depends on this choice. The densities and viscosities used in this simulation are  $\rho_k = 1$ ,  $v_1 = 1/6$ ,  $v_2 = 1/96$ ,  $v_3 = 1/3$ ,  $v_4 = 1/192$ ,  $v_5 = 2/3$ , and  $v_6 = 1/24$  respectively.

The numerical velocity profile that was obtained at steady state is compared in Fig. (15) to the theoretical profile for each of the possible viscosity interpolations considered in this study. Let us denote as  $E(x_j)$  the difference between the numerical

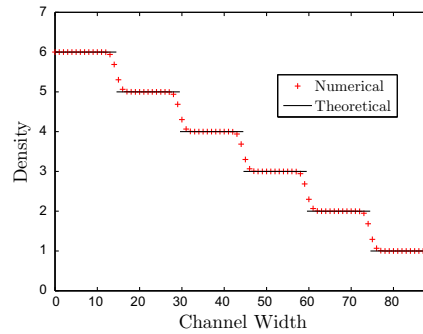
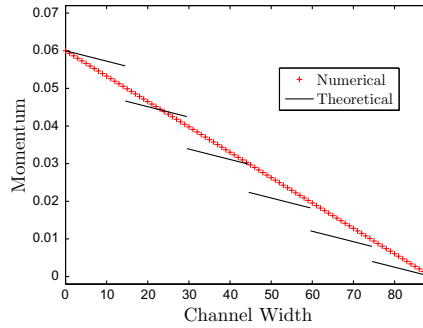
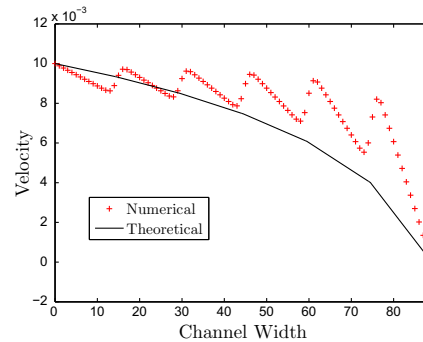
and theoretical velocity of the fluid at site  $x = x_j$ . Table 10 shows the error with the theoretical profile using different norms. A norm is calculated with all the lattice sites. Clearly, from Fig. 15 and Table 10, the  $q$ -average with  $q = -1$  used to compute  $\bar{v}|_q$  provides better results than the other alternatives. Afterwards, the accuracy decreases as  $q$  increases. The numerical profile in Fig. 15(a) agrees better with the theoretical profile than that in Figs. 15. Moreover, for some norms, errors can be lowered by one order of magnitude compared to other choices for  $\bar{v}|_q$ , and for the same lattice size.

From Section (3.2), the  $q$ -average with  $q = 2$  was the best choice. This leads to a kind of contradiction, however. The planar interface simulations tell us to take  $q = 2$ , while the Couette's flow tells us to take  $q = -1$ . We think that  $q = -1$  is a bet-

**Table 10**

Error comparison based on different norms for the multilayered Couette's flow with unit density ratios.

	$\omega_{\text{eff}}$ calculated with $\bar{v} _q$			
	$q = -1$	$q = 0$	$q = 1$	$q = 2$
$\max  E(x_i) $	8.785e-05	2.744e-04	6.115e-04	8.848e-04
$\frac{1}{N-N_0} \sqrt{\sum_i (E(x_i))^2}$	2.218e-06	9.505e-06	2.254e-05	3.678e-05
$\frac{1}{N} \sum_i  E(x_i) $	7.304e-06	6.762e-05	1.645e-04	2.782e-04

(a) Density profile  $\rho$ .(b) Momentum profile  $\rho \vec{u}$ .(c) Velocity profile  $\vec{u}$ .**Fig. 16.** Numerical and theoretical solution profile for the multilayered Couette's flow with variable density ratios.



ter choice when simulating unit density ratio, and  $q = 1$  appears to be the better choice when dealing with a non unit density ratio. Nevertheless, there are still many factors that are not taken into account, and the accuracy resulting from the viscosity interpolation may depend more on the type of flow than we may think. Thus, depending on what is most important, e.g. surface tension or velocity, other choices might be better suited to a given situation.

### 3.5.2. Multilayered Couette's flow with variable density ratios

In this section, the current model is tested against the multilayered Couette's flow with variable density ratios between the fluid interfaces. The density and viscosity of the different fluids are  $\rho_k = 7 - k$  and  $\nu_k = 1/6$ .

It turns out that the model fails this numerical test. In [36], it was shown that an RK model fails the multilayered Poiseuille's flow with variable density ratios. Poiseuille's flow is more complicated than Couette's flow, because of the source term involved in the model that mimics a pressure gradient. In an earlier work [13], failure of the Poiseuille's flow test was blamed on a possible inaccuracy of the source term in the presence of variable density ratios. It is possible that this hypothesis may not be correct, because, even though no source term is needed to simulate Couette's flow, the model is still unsuccessful. Note that Poiseuille's flow, which is a similar problem, can be simulated with very high viscosity ratios,  $O(10000)$ , as long as the unit density ratio is considered [13].

The numerical solution for the density, velocity, and momentum is presented with the analytical solution in Fig. (16). At steady state, the numerical density profile matches the theoretical profile, but the numerical velocity and the momentum profile are incorrect.

From Fig. (16(b)), we can realize that momentum decreases smoothly and linearly from the left to the right boundary, without being affected **at all** by the change in the fluid density across the interface. This shows the model's inability to simulate flow with variable density ratios in the presence of non zero momentum or a non zero momentum gradient. In all the preceding test cases, the analytical solution at steady state was calculated with zero momentum. This may well explain why these test cases provide good results at steady state, but not for the Couette's flow with variable density ratios. Note that the validity of the unsteady process at high density ratios in the earlier test cases is also open to discussion.

It should be pointed out, however, that the numerical density profile in Fig. (16(a)) is correct, and that it agrees well with the fact that previous tests only investigated the model's behavior in terms of density. First, in Section (3.3), the pressure jump is linearly related to density with the equation of state in Eq. (11). Second, in order to introduce surface tension, the role of the perturbation operator is to deplete mass (density behavior) perpendicular to the color gradient and add mass in the direction of the color gradient *while conserving momentum*. Third, the special interface thickness adjustment set by Eq. (28) only adjusts to the different color density profile. All the previous tunings seem to work well with variable density ratios with a momentum that is theoretically zero. However, when a variable density ratio is simulated along with non zero momentum or a non zero momentum gradient, this RK model fails.

In the [36] study, an RK [36], an SC [36], an FE [37,38], and an MF [39] model were tested against a three-layer Poiseuille's flow with variable density ratios. None of these models passed the test. Moreover, it is thought that they would also fail the simpler Couette's flow test with variable density ratios. In this respect, we have not been able to find a study in the reviewed literature which discusses a successful simulation obtained with a pure LB model. There is one exception, however, which we found in the Knutson and Noble [40] paper, where this basic flow was successfully simulated. Nevertheless, the authors clearly state that their method, as presented, is not suitable for more complicated flow configurations. A great deal of effort is still needed to generalize their method to solve general complex flows. Moreover, this method may need to be combined with a level set solver, which would mean that the elegance of a pure LB model would be lost.

From the above results, we conclude that there remains a missing link for pure multiphase LB schemes with variable density ratios, and that, unfortunately, these schemes may not be ready for engineering applications. However, for applications where density ratios can be neglected, i.e. unit density ratios, this numerical scheme works very well.

## 4. Technical details

This section is included to explain how this numerical algorithm can be constructed in such a way that the computer memory required is significantly reduced. This is an important factor to take into account when simulating  $N$ -phase flow when  $N$  is large. The pseudo-algorithm for the LB model in this paper is the following:

1. Initialization of the density field  $\rho_k$  for each fluid  $k$ .
2. Initialization of the color-blind distribution functions  $N_i$ . Usually,  $N_i$  is initialized with the equilibrium:

$$N_i|_{t=0} = \sum_k N_i^{k(e)} \quad (64)$$

It is important to note the following property of the color-blind equilibrium:

$$N_i^{(e)} = \sum_k N_i^{k(e)}(\rho_k, \vec{u}, \alpha_k) = N_i^{(e)}(\rho, \vec{u}, \vec{\alpha}|_{q=1}) \quad (65)$$

3. Main loop:

- BGK collision on the color-blind distribution functions  $N_i$  using the effective relaxation factor  $\omega_{\text{eff}}$ . Note that:

$$(\Omega_i)^{(1)}(N_i) = \sum_k (\Omega_i^k)^{(1)}(N_i^k) = \sum_k N_i^k - \sum_k \omega_{\text{eff}}(N_i^k - N_i^{k(e)}) = N_i - \omega_{\text{eff}}(N_i - N_i^{(e)}) \quad (66)$$

It is from the previous equation that we realize how important it is to choose the same  $\omega_{\text{eff}}$  for each fluid color. Without this, the previous equation does not hold and the BGK collision cannot be performed only on the color-blind distribution functions.

- Compute and store the gradient of the color density fraction  $\vec{\nabla} \left( \frac{\rho_k}{\rho} \right)$  for each fluid  $k$ .
- Apply the perturbation to the color-blind distribution functions  $N_i$ . Note that:

$$(\Omega_i)^{(2)}(N_i) = \sum_k (\Omega_i^k)^{(2)}(N_i^k) = N_i + \sum_k \sum_{l \neq k} \frac{A_{kl} C_{kl}}{2} |\vec{F}_{kl}| \left[ W_i \frac{(\vec{F}_{kl} \cdot \vec{c}_i)^2}{|\vec{F}_{kl}|^2} - B_i \right] \quad (67)$$

- Set  $N_i^{\text{temp}} = 0$  and  $\rho_k^{\text{temp}} = \rho_k$ .
- Loop over each fluid  $k$ :
  - Recolor fluid  $k$  in order to obtain  $N_i^k$  using the recoloring operator  $(\Omega_i^k)^{(3)}$ , the fluid density of each fluid  $\rho_k^{\text{temp}}$ , and the color-blind distribution functions  $N_i$ .
  - Stream the distribution functions  $N_i^k$  using the streaming operator  $(\Omega_i^k)^{(4)}$ .
  - Store the new values for the density and color-blind distribution functions:

$$N_i^{\text{temp}} = N_i^{\text{temp}} + N_i^k \quad (68)$$

$$\rho_k = \sum_k N_i^k \quad (69)$$

So, the idea of the previous loop is to recolor and stream one fluid color at a time.

- Set  $N_i = N_i^{\text{temp}}$ .

The previous pseudo-procedure implies that, for each fluid color  $k$ , the density  $\rho_k$ , the gradient of the density fraction  $\vec{\nabla} \left( \frac{\rho_k}{\rho} \right)$ , and the color-blind distribution functions  $N_i$  for each lattice site needs to be always kept in memory. Depending on the software implementation, a temporary copy of these variables may also need to be kept in memory. What is important to note is that there is no need to always store the distribution functions  $N_i^k$  of each fluid  $k$ , but only their density  $\rho_k$ .

In addition, the use of sparse arrays could be used for each fluid  $\rho_k$  and the gradient of the density fraction  $\vec{\nabla} \left( \frac{\rho_k}{\rho} \right)$ , in order to reduce the total computer memory required. Of course, this would be at the expense of losing mass conservation, but this may be controlled. Moreover, if the norm of the color gradient is near zero for a certain  $k$ - $l$  fluid interface, the value  $\beta_{kl}$  could be set to zero to decrease the computational complexity of the recoloring operators. The same strategy can be applied for the perturbation operator by setting  $A_{kl} = 0$ , if the color gradient is negligible. All these numerical techniques will be studied in a future work and have not been applied here.

## 5. Conclusion

In this paper, a lattice Boltzmann model for the simulation of multiple immiscible fluids was developed and numerically investigated. Our results show that, as long as the momentum is theoretically zero at steady state, the model can effectively simulate high density and high viscosity ratios, up to  $O(1000)$  and  $O(100)$  respectively, with stability and accuracy. In spite of this success, the multilayered Couette's flow with variable density ratios is a test case that the current model fails to simulate. However, for unit density ratios, this model appears to be very accurate. The generalization from two phases to  $N$  phases is not straightforward, because all the collision operators need to be generalized for  $N$  phases and still capture some of the essential physics. Particular attention has been paid to the definition of the color gradient, in order to avoid numerical instability and non physical mass flow tangential to the interfaces. Fortunately, there was a definition of that vector in the Allen-Cahn system that works properly. Moreover, this definition has the advantage of generalizing the model to  $N$ -phase flows while only using neighbor information with  $O(N)$  in computational complexity. Also, the concentration factor in our model, which is used to limit the activation of the surface tension to the desired interface, and which is absent in the two-phase flow simulation, is carefully selected. The choice of the effective relaxation factor seems to be an important factor affecting the accuracy of the model as well. For three-phase flow, the interface width at the triple fluid junction must be considered in a special way, in order to capture the correct static contact angles. All the previous details were needed, even for unit density ratios, to correctly embed Laplace's law and Laplace–Young's law in this  $N$  phase LB model. This LB model can be constructed in such a way that there is no need to keep all the various color distribution functions in memory, as only the color-blind distribution functions are needed. We believe that this model may be able to achieve both high density and high viscosity ratios up to  $O(1000)$  simultaneously for several test cases. When simulating high viscosity ratios, to avoid a large over-relaxation of the effective relaxation parameters, one of the fluid viscosities must be very low, which might cause instability. The BGK collision operator, as used in this work, is known to result in unstable simulation for low viscosity. Other collision operators like the two-relaxation time (TRT) operator [41] or the multi-relaxation time (MRT) operator [42], which behave better

in such situations, might solve this problem. The introduction of the Brownlee et al. stability condition into this model could also help [43]. Another alternative might be the entropic lattice Boltzmann methods [44]. It would be interesting to investigate these options in future work. Also, further research needs to be conducted to find a cure for the discontinuity problem of the multiphase LB model [45] and allow high density ratios to be accurately simulated in the multilayered Couette's flow. For now, this model can only be used with confidence when the various density ratios can be neglected and set to unity.

## Acknowledgments

This work was supported by a grant from the NSERC (Natural Sciences and Engineering Research Council of Canada) and FQRNT (Le Fonds Québécois de la Recherche sur la Nature et les Technologies). We applied the SDC (sequence-determines-credit) approach in listing the authors of this article [46].

## References

- [1] D.H. Rothman, J.M. Keller, *Journal of Statistical Physics* 52 (1988) 1119–1127.
- [2] A.K. Gunstensen, D.H. Rothman, S. Zaleski, G. Zanetti, *Physical Review A* 43 (1991) 4320.
- [3] X. Shan, H. Chen, *Physical Review E* 47 (1993) 1815.
- [4] M. Swift, E. Orlandini, W.R. Osborn, J.M. Yeomans, *Physical Review E* 54 (1996) 5041.
- [5] X. He, X. Shan, G.D. Doolen, *Physical Review E* 57 (1998) R13.
- [6] L.O.E. Santos, P.C. Facin, P.C. Philippi, *Physical Review E* 68 (2003) 056302.
- [7] J. Bao, L. Schaefer, *Applied Mathematical Modelling*.
- [8] S. Gokaltun, D. McDaniel, Multiple-relaxation-time lattice boltzmann method for multiphase flows with high density ad viscosity ratios - 10135, 2010.
- [9] T. Reis, T.N. Phillips, *Journal of Physics A: Mathematical and Theoretical* 40 (2007) 4033–4053.
- [10] D. Grunau, S. Chen, K. Eggert, *Physics of Fluids A: Fluid Dynamics* 5 (1993) 2557–2562.
- [11] U. D'Ortona, D. Salin, M. Cieplak, R.B. Rybka, J.R. Banavar, *Physical Review E* 51 (1995) 3718–3728.
- [12] M. Latva-Kokko, D.H. Rothman, *Physical Review E* 71 (2005) 056702.
- [13] S. Leclaire, M. Reggio, J.-Y. Trépanier, *Applied Mathematical Modelling* 36 (2012) 2237–2252.
- [14] S. Leclaire, M. Reggio, J.-Y. Trépanier, *Computers & Fluids* 48 (2011) 98–112.
- [15] A.K. Gunstensen, *Lattice-Boltzmann Studies of Multiphase Flow Through Porous Media*, Ph.D. thesis, 1992.
- [16] M.M. Dupin, I. Halliday, C.M. Care, *Journal of Physics A: Mathematical and General* 36 (2003) 8517–8534.
- [17] I. Halliday, A.P. Hollis, C.M. Care, *Physical Review E* 76 (2007) 026708.
- [18] T.J. Spencer, I. Halliday, C.M. Care, *Physical Review E* 82 (2010) 066701.
- [19] J. Tölke, *Philosophical Transactions of the Royal Society of London, Series A: Mathematical Physical and Engineering Sciences* 360 (2002) 535–545.
- [20] F.M. van Kats, P.J.P. Egberts, C.P.J.W. van Kruisdijk, *Transport in Porous Media* 43 (2001) 225–238.
- [21] I. Halliday, S.P. Thompson, C.M. Care, *Physical Review E* 57 (1998) 514.
- [22] H. Garcke, B. Nestler, D. Stoth, *SIAM Journal on Applied Mathematics* 60 (1999) 295–315.
- [23] S. Leclaire, M. El Hachem, M. Reggio, in: *MATLAB, A Fundamental Tool for Scientific Computing and Engineering Applications*, vol. 3, InTech, 2012.
- [24] M. Sbragaglia, R. Benzi, L. Biferale, S. Succi, K. Sugiyama, F. Toschi, *Physical Review E* 75 (2007) 026702.
- [25] A. Kawasaki, J. Onishi, Y. Chen, H. Ohashi, *Computers & Mathematics with Applications* 55 (2008) 1492–1502.
- [26] A.J. Briant, J.M. Yeomans, *Physical Review E* 69 (2004) 031603.
- [27] F.J. Alexander, S. Chen, D.W. Grunau, *Physical Review B* 48 (1993) 634.
- [28] I. Ginzbourg, P.M. Adler, *Transport in Porous Media* 20 (1995) 37–76.
- [29] R. Mei, L.-S. Luo, P. Lallemand, D. d'Humières, *Computers & Fluids* 35 (2006) 855–862.
- [30] J. Kim, *Interfaces and Free Boundaries* 7 (2005) 435–466.
- [31] F. Boyer, C. Lapuerta, S. Minjeaud, B. Piar, M. Quintard, *Transport in Porous Media* 82 (2010) 463–483.
- [32] J. Lätt, *Hydrodynamic limit of lattice Boltzmann equations*, Ph.D. thesis, 2007.
- [33] P.K. Jain, *Simulation of two-phase dynamics using lattice Boltzmann method (LBM)*, Ph.D. thesis, 2010.
- [34] G.K. Batchelor, *An introduction to fluid dynamics*, Cambridge Mathematical Library series, Cambridge University Press, 1967.
- [35] Q. Zou, X. He, *Physics of Fluids* 9 (1997) 1591–1598.
- [36] G. Rannou, *Lattice-Boltzmann method and immiscible two-phase flow*, Master's thesis, 2008.
- [37] E. Orlandini, M.R. Swift, J.M. Yeomans, *EPL (Europhysics Letters)* 32 (1995) 463.
- [38] H.W. Zheng, C. Shu, Y.T. Chew, *Journal of Computational Physics* 218 (2006) 353–371.
- [39] X. He, S. Chen, R. Zhang, *Journal of Computational Physics* 152 (1999) 642–663.
- [40] E. Knutson, C.R. Noble, D., *European Physical Journal, Special Topics*, 171 (2009) pp. 21–29.
- [41] I. Ginzburg, *Journal of Statistical Physics* 126 (2007) 157–206.
- [42] K.N. Premnath, J. Abraham, *Journal of Computational Physics* 224 (2007) 539–559.
- [43] R.A. Brownlee, A.N. Gorban, J. Levesley, *Physical Review E* 75 (2007) 036711.
- [44] B.M. Boghosian, J. Yepez, P.V. Coveney, A. Wager, *Proceedings of the Royal Society of London, Series A: Mathematical Physical and Engineering Sciences* 457 (2001) 717–766 (10.1098/rspa.2000.068).
- [45] C.K. Aidun, J.R. Clausen, *Annual Review of Fluid Mechanics* 42 (2010) 439.
- [46] T. Tschardt, M.E. Hochberg, T.A. Rand, V.H. Resh, J. Krauss, *Author sequence and credit for contributions in multiauthored publications*. *PLoS Biol* 5 (2007) e18. available at: <http://www.plosbiology.org/article/info%3Adoi%2F10.1371%2Fjournal.pbio.0050018>.